THE DOUBLE-HERALDED GENERATION AND FREQUENCY TRANSLATION OF TWO-PHOTON STATES OF LIGHT IN OPTICAL FIBERS

by

ROGER A. SMITH

A DISSERTATION

Presented to the Department of Physics
and the Graduate School of the University of Oregon
in partial fulfillment of the requirements
for the degree of
Doctor of Philosophy

September 2016

DISSERTATION APPROVAL PAGE

Student: Roger A. Smith

Title: The Double-Heralded Generation and Frequency Translation of Two-Photon States of Light in Optical Fibers

This dissertation has been accepted and approved in partial fulfillment of the requirements for the Doctor of Philosophy degree in the Department of Physics by:

Daniel A. Steck	Chair
Michael G. Raymer	Advisor
Eric I. Corwin	Core Member
Andrew H. Marcus	Institutional Representative

and

Scott L. Pratt	Dean of the Graduate School

Original approval signatures are on file with the University of Oregon Graduate School.

Degree awarded September 2016

DISSERTATION ABSTRACT

Roger A. Smith

Doctor of Philosophy

Department of Physics

September 2016

Title: The Double-Heralded Generation and Frequency Translation of Two-Photon States of Light in Optical Fibers

The creation of optical states of light that are quantum mechanical in nature in optical fibers is discussed and demonstrated experimentally. Specifically, two-photon states created by spontaneous four-wave-mixing in commercially available single-mode, birefringent fibers are studied. When creating photon states of light, it is important to verify the created states are of the proper photon number distribution and free of noise. We detail a method for combining thresholding, non-number resolving detectors to characterize the photon number distribution created via SFWM and a procedure to quantify the noise sources present in the process. Frequency translation in optical fibers with two-photon states is discussed and experimental considerations are presented.

CURRICULUM VITAE

NAME OF AUTHOR: Roger A. Smith

GRADUATE AND UNDERGRADUATE SCHOOLS ATTENDED:

University of Oregon, Eugene, OR
University of Rochester, Rochester, NY

DEGREES AWARDED:

Doctor of Philosophy, Physics, 2016, University of Oregon
Master of Science, Physics, 2010, University of Oregon
Bachelor of Science, Optics, 2009, University of Rochester
Bachelor of Arts, Physics, 2009, University of Rochester

AREAS OF SPECIAL INTEREST:

Nonlinear Optics, Lasers, Quantum Optics, Optical Fibers

PROFESSIONAL EXPERIENCE:

Research Assistant, University of Oregon, 2010-2016

Teaching Assistant, Graduate Internship Program Optical Materials and Devices Track, 2014-2015

NSF GK-12 Fellow, University of Oregon, 2012-2014

Teaching Assistant, University of Oregon, 2009-2010

GRANTS, AWARDS AND HONORS:

Weiser Senior Teaching Award, University of Oregon, 2015

Honorable Mention, Student Poster Competition, Siegman International School on Lasers, 2014

University Stoddard Prize, University of Rochester, 2009

President's Award for Undergraduate Research, University of Rochester, 2009

PUBLICATIONS:

R.A. Smith, D.V. Reddy, D.L.P. Vitullo, and M.G. Raymer, "Double-heralded generation of two-photon-states by spontaneous four-wave-mixing in the presence of noise." *Optics Express* **24**, 5809-5821 (2016).

R. A. Smith, D. V. Reddy, D. L. Vitullo, and M. G. Raymer, "Verification of a heralded, two-photon fock state with a gang of ddetectors." *Frontiers in Optics (FiO'15)*, OSA Technical Digest, paper FTu3G.2 (2015).

L.J. Bissell, S.G. Lukishova, R.A. Smith, M. Lahiri, C.R. Stroud Jr., and R.W. Boyd, "Polarized single photons from colloidal quantum dots in chiral microcavities at room temperature." *International Quantum Electronics Conference (IQEC'09)*, OSA Technical Digest, paper ITuJ5 (2009).

ACKNOWLEDGEMENTS

I thank my advisor, Dr. Michael G. Raymer for the supervision and guidance. The countless hours he spent providing advice, helping me work through complex problems in quantum optics, and general discussions of the underlying philosophy of physics have been invaluable to my education as a scientist and as a member of society. I am grateful for the opportunity to work in his lab and learn from him these last few years. This experience has been an absolute treat, at times quite trying, but highly rewarding and I am honored to call my time in the Raymer lab the foundation of my career.

I thank Dr. Daniel Steck and Dr. Andrew Marcus for the many helpful discussions regarding my research and other topics in optics and chemistry. I thank Dr. Eric Corwin for the many hours of discussion (or hours of me not understanding) statistics and other topics of physics and the finer points of whiskey and firearm control in the state of Oregon. Much gratitude is deserved by all the administrative people that have helped ensure all the little details are always fulfilled. Many thanks to Stan Micklavzina and the other demo room workers for lending me countless pieces of equipment for public demos, my work, or just for fun.

Many thanks to my fellow Raymer labmates, from whom I have learned so many things in and out of the lab. Being surrounded by upstanding people with strong intellects has made the process a little easier and much more enjoyable: Dr. Hayden McGuinness, Kyle Lynch-Klarup, and Erin Mondloch. Sepcial thanks go to Dash Vitullo and Dileep Reddy, who were always patient in explaining various theories and willingly spent many late nights in the lab, making those long hours

in the middle of the night easier to bear. I am certain that I will look back on my time with all of you with fond memories and a high standard of a collegial working environment.

It is impossible to acknowledge all those that have helped me achieve this goal. My successes demonstrated here are not mine alone, but accompanied by the collective effort of countless numbers of teachers, mentors, friends, and family that have helped me learn about the world and given me opportunities to explore my curiosity. I am greatly indebted to my parents, Roger and Ann Smith, without whom none of this would be possible. For providing me the opportunities early on to learn about science and mathematics, and always being my loudest advocate while pushing me ever further. My sister, Stephanie, is equally to blame by always pushing me to succeed academically with her own accolades, always outnumbering my own.

There have been many friends that have helped ease the difficulties and pains in studying quantum optics and helped in creating beautiful memories during this degree. My time in Eugene has been enriched with so much joy from far too many people to list here. But I would be remiss not to acknowledge a few that have been there for me, through and through. To Rick Montgomery for the endless nights of rabbit hole intellectual excursions and Peter Morse for always reminding me that there is a cat on the internet exuding my emotions better than me, thank you for your deep friendship and support. And to Marie Conley for her endless encouragement and love, who helped keep me going toward the end of this journey.

For my educators, who fed my curiosity and opened my eyes to the infinite world of possibilities.

TABLE OF CONTENTS

LIST OF FIGURES

LIST OF TABLES

Table Page

CHAPTER I

INTRODUCTION

Roughly one hundred years ago, a revolution was in the early, sleepy beginnings that only a truly paradigm-shifting theory can hold. The adoption of this new belief was slow and wrought with confusion and contradiction. At the crux of the revolution was a change in humans' fundamental understanding of the mechanics of the universe. Contrary to how the world appears in the everyday existence that humans enjoy, the deepest reality is not deterministic, but probabilistic. This is the apparent contradiction at the root of quantum mechanics (that is not much of a contradiction, after all).

The philosophical interpretation of quantum mechanics, a world built upon probabilities, seemed so inconsistent with reality that Albert Einstein famously denounced the theory, a theory of which he was a principal architect. Forms of his famous statement remains well popularized today: God does not play dice with the universe.[1] There have been many summits full of the best and brightest minds in physics, chemistry, and philosophy to understand the implications of such a theory. Many questions have arisen, along with many answers, although not always clear.

The history of quantum mechanics is long and rich, far more than will be covered here. Instead, we will connect some of the highlights that are particularly interesting or illuminating.[2] Max Planck is credited with originally postulating the idea of a discrete amount of energy, or quanta, to explain the behavior of

[1]To which Niehls Bohr responded with a reprimand similar to "stop telling God what to do."

[2]It should also be noted that some of the elementary ideas of quantum mechanics are very similar to ideas presented by some philosophers of ancient Greece. The curious reader is directed to works by Werner Heisenberg for further discussion of these ideas [1].

blackbody radiation. A blackbody is a mass that absorbs all incoming light and appears black at room temperature, hence the name. As a blackbody absorbs light, its temperature rises, and it begins to emit the light. Prior to Planck's theory, there was a significant discrepancy between the observation of blackbody radiation and the theories of the time, called the ultraviolet (UV) catastrophe. Previous studies theorized that the radiation from a blackbody would by skewed toward higher energies, putting the peak of radiation in the ultraviolet. Planck's modification to existing theory caused the peak to move toward lower energies and matched the observed radiation spectrum extremely well.

Four years later, Einstein expanded the discretization of energy and electromagnetic radiation to the interaction with metals through the theory of the photoelectric effect. In 1921, Einstein was awarded a Nobel prize for this discovery. The photoelectric effect opened the door for matter-light interactions in the quantum regime. Six years after Einstein's Nobel prize, Paul A.M. Dirac took quantum matter-light interactions further through the development of a theory of quantum radiation and absorption that won him the Nobel prize in 1933.

Although quantum mechanics was a quickly growing field in the first half of the twentieth century, certain theoretical results were not able to be shown experimentally, especially in the field of nonlinear optics. Nonlinear optics required a high energy light beam to interact with a material to exploit the nonlinear response from the medium. A transparent material typically exhibits linear behavior when light interacts with it (e.g. light traveling through a glass window pane). However, the polarization of the material has a nonlinear component that is many orders of magnitude lower than the linear response. With the successful demonstration of the MASER (Microwave Amplification by Stimulated Emission of

Radiation) in 1954 by Charles Townes, James P. Gordon, and H. J. Zeiger, and the LASER built in 1960 by Theodore Maiman, the world of experimental nonlinear optics was born. In 1961, the first demonstration of nonlinear effects was shown by Franken *et al.* in crystalline quartz [2]. In 1967, Stephen Harris and colleagues observed optical parametric fluorescence in a lithium niobate crystal [3]. Three years later, David Burnham and Donald Weinberg demonstrated spontaneous parametric downconversion in an ammonium dihydrogen phosphate crystal [4].

The nonlinear effects observed in the 1960s were inherently quantum mechanical in nature. In 1956, Hanbury-Brown and Twiss performed a key experiment that illustrated a method for measuring correlations between different beams of light [5]. The Hanbury-Brown and Twiss setup would become a powerful tool for quantum optics experiments. A proper formalism for quantum optics was developed by Roy J. Glauber in 1963 that elucidated the statistical properties of quantum states of light, which are much different from classical light [6]. Nearly two decades later, Kimble, Dagenais, and Mandel confirmed the non-classical behavior of light emitted from sodium atoms excited with a laser [7]. Short and Mandel further measured the sub-Poissonian statistical nature of photons in 1980 [8]. Grangier *et al.* measured the second-order coherence of heralded single photons [9]. The same year using two-photon interference, Hong, Ou, and Mandel experimentally determined the temporal duration of photons produced by spontaneous downconversion in a KDP crystal to be of the order of femtoseconds, or 10^{-15} seconds [10]. This technique, termed Hong-Ou-Mandel interference, has become standard practice in experimental quantum optics to determine the indistinguishability of quantum states.

Since the demonstration of Hong-Ou-Mandel interference, the field of quantum optics has grown rapidly, including the creation of various subfields such as quantum information processing and quantum computation. Various protocols for sending information encoded in quantum states have been invented [11, 12] and experimentally demonstrated [13, 14, 15]. The field of the quantum information technology has become such a mature field that there are commercial products available from a number of companies to provide secure transfer of information with quantum protocols.

In 1995, Peter Shor proved the ability of a quantum computer to factor very large numbers, a task a classical computer is unable to complete [16]. Algorithms for quantum computers were expanded by Grover in 1997 [17]. Experimental realization of quantum bits were shown by a variety of groups in ions [18], trapped atoms [19], and the atomic spin [20, 21]. This was followed by the first demonstration of a quantum algorithm in 1998 by Jones, Mosca, and Hansen in nuclear magnetic spins [22]. A landmark paper was presented in 2001 by Knill, Laflamme, and Milburn describing an experimental protocol for quantum computation with linear optics [23]. In the two centuries after this result, many forms of creating optical qubits have been shown including the first demonstrations of all optical controlled-NOT gates in 2003 by Pittman *et al.* and O'Brien *et al.* [24, 25]. As with quantum information protocols, there has been a significant interest in the commercialization of quantum computation, with applications primarily in encryption. Quantum computation and quantum information sciences continue to grow at a dizzying pace, without any slowing in sight.

In tandem with the beginnings of quantum optics, optical fibers were being developed for sending information via classical light. The optical fiber

was first demonstrated by Charles Kao and George Hockham in 1966 [26]. The use of light for classical communication in optical fibers spawned another field, telecommunications, which is the backbone of countless services and technology that are ubiquitous today. In contrast to the field of telecommunications, we are interested in the nonlinear effects of optical fibers with intense laser pulses. Optical fibers create photon states that are tailorable, depending on the properties of the fiber including length and the spectral profile of the pump [27, 28]. This dissertation is focused on the intersection of quantum optics and nonlinear optics in optical fibers, with an emphasis on the creation, detection, and frequency translation of quantum states of light.

In this dissertation, we explore the underpinnings of the processes involved in creating and manipulating photon pairs in optical fibers. First, in Chapter II, we will begin with a discussion of essential quantum optics necessary for this dissertation, which is one small part of the rich, complex world of quantum mechanics. We begin with the fundamental equations that govern the behavior of light, Maxwell's equations. By quantizing Maxwell's equations, we move from the classical regime into the quantum regime and can explore the behavior of light at the single photon level. A brief introduction into quantum optics will be presented followed by a discussion of a common measurement in determining the number of photons present, the second-order correlation function measurement, $g^{(2)}(\tau)$.

From quantum optics, we move into exploring the medium of interest in this work, the optical fiber. Chapter III begins again with Maxwell's equations, although modified to describe the behavior of light in a medium. We discuss the effects of the medium on the propagation of light and derive the nonlinear Schrödinger equation in a fiber. From expanding the response of the medium, we

are able to uncover the nonlinear nature of the medium, opening the possibility to explore various nonlinear phenomena. Simply put, these phenomena result from the interaction of the optical fiber to redistribute the energy from the incident light waves, to waves of different frequencies. Particular attention is given to the process of creating photon pairs and to the scattering of an incident photon, called modulation instability and Bragg scattering, respectively. Modulation instability is studied in commercially available, birefringent step-index fiber, while Bragg scattering is examined in the context of using photonic crystal fibers. Birefringent fibers have become a common source for photon-pair generation [28, 29, 30, 31]. We will discuss methods to tailor the spectral correlation of photon pairs produced in birefringent fibers. Photonic crystal fibers have opened a world of nonlinear optics across the visible spectrum [32, 33, 34, 35, 36]. We are concerned mainly with using photonic crystal fibers for frequency translation [37].

In Chapter IV, we consider the prospect of verifying two-photon states created in optical fibers. The process of heralding, or conditional preparation, is used to produce pairs of photons. In this scheme, one photon from the pair is detected to "herald" the presence of the other photon, drastically reducing the effects of noise or empty counts in single-heralded photon pair generation. However, moving to double-heralded two-photon states requires careful examination to distill the photon number distribution in the presence of noise. We present methods for effectively quantifying the contribution from different noise processes and recovering the noise-free distribution that would be created if the noise was properly filtered experimentally. This technique is a powerful tool in understanding the noise present in double-heralded photon generation.

After creating and verifying double-heralded two-photon states, we explore the outcomes of performing Bragg scattering on these states in Chapter V. As shown in Chapter III, Bragg scattering is analogous to a beam splitter with the two output ports consisting of the different frequency bands rather than two different output directions from a beamsplitter. Put another way, Bragg scattering in a fiber is analogous to a moving Bragg grating that couples two frequency channels together. Through this formalism, it is straightforward to discuss the effects of performing frequency translation on a two-photon state. We describe the process with different input states and show the necessity for high efficiency and care when calculating the final output states.

We conclude this exploration into the process of photon generation and nonlinear quantum optics in Chapter VI. Although the work presented here is a small set of the current work in the field of quantum optics, it provides a background for further exploration into photon pair sources and other quantum nonlinear effects in $\chi^{(3)}$ materials as well as a flavor of the considerations needed to measure the photon-number distribution created from nonlinear sources.

CHAPTER II

QUANTUM STATES OF LIGHT

The concept of the photon, or a single quantum of light, is one of the many advances that arose from the work of Planck and Einstein in the early twentieth century. The term photon was originally coined in 1917 by Leonard Troland in his studies of the absorption of the retina and human visual perception [38].[1] The fundamental physical meaning of a photon is often difficult to elucidate in experiments of quantum optics. Rather, operational definitions are often adopted to provide some understanding (e.g. a single detection or "click" of a detector). Indeed, much care must be taken when using the word photon to describe a single quantum of energy.

In the face of some haste in terminology, quantum optics has become a beautifully complex and diverse field at the intersection of optics and quantum effects. Fortunately, much of the formalism of quantum optics follows from classical optics with some modifications. This chapter will examine a small field of quantum mechanics, focused on the behavior of photons. We are interested in quantum states of light, especially the distributions created by sources, the spectral properties of the photons created by these sources, and nonlinear interactions involving photons. Following a brief introduction into quantum states, we will describe types of measurements of quantum states typically performed in the laboratory.

[1]The introduction of the word "photon" is often attributed to Gilbert N. Lewis from his 1926 Nature paper [39], although it appears first in Troland's 1917 paper on visual perception. The interested reader is directed to a recent paper on the history of the term by Helge Kragh [40]

2.1. The Harmonic Oscillator

In classical physics, a typical problem studied is the simple harmonic oscillator. A simple harmonic oscillator is a pendulum or a mass on a spring bouncing back and forth as shown in Fig. 2.1. To have a harmonic oscillator, it is necessary to have a restoring force opposing the motion of the mass. For the spring, this is the spring pulling the mass toward equilibrium and in a pendulum the restoring force is gravity, pulling the mass to the bottom of the arc.

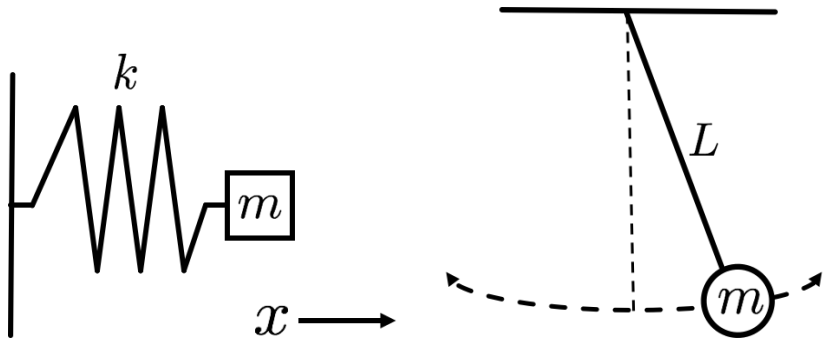

FIGURE 2.1. (a) A mass, m, on a spring with a spring constant k. The spring force opposes the motion of the mass toward the equilibrium point, causing spring to oscillate. (b) A pendulum composed of a mass, m, on a string of length L. Gravity pulls the mass to the lowest point, causing the mass to oscillate. Both the mass on a spring and pendulum are examples of simple harmonic oscillators.

As an illustration, let us examine the case of a mass on a spring, shown in Fig. 2.1(a). Let the mass be m and the spring have a constant of k. We assume everything is in one direction, so the vector nature of the force and displacement are simplified to scalars with implicit direction along $\vec{x}$. The spring exerts a force on the mass proportional to the displacement from equilibrium

$$F(x) = -kx. \tag{2.1}$$

From Newton's second law, the force is equal to mass times acceleration, or the second time derivative of displacement. Using this relation and the equation for momentum, we can describe the equations of motion for the mass

$$m\frac{d^2x}{dt^2} = -kx \tag{2.2}$$

$$p_x = m\frac{dx}{dt}. \tag{2.3}$$

By solving the differential equations Eqs. 2.2 and 2.3, we have the behavior of the spring in time

$$x(t) = x_0 \sin(\omega t) \tag{2.4}$$

$$p_x(t) = m\omega x_0 \cos(\omega t), \tag{2.5}$$

where x_0 is the equilibrium point and ω is the frequency of oscillation. The value for the frequency follows from the original equations of motion

$$\omega = \sqrt{\frac{k}{m}}. \tag{2.6}$$

The energy stored in the spring is described by the Hamiltonian, which is the sum of the kinetic, T, and potential V, energies. The equations for the kinetic and potential energies are given by

$$T = \frac{1}{2}m\left(\frac{dx}{dt}\right)^2 = \frac{p_x^2}{2m} \tag{2.7}$$

$$V = \frac{1}{2}kx^2 = \frac{1}{2}m\omega^2x^2, \tag{2.8}$$

where the kinetic energy was written in terms of the momentum. Eq. 2.8 is valid for conserving forces, or forces that are independent of the path taken during motion. The Hamiltonian for this spring is then

$$\mathcal{H} = \frac{p^2}{2m} + V(x) = \frac{p^2}{2m} + \frac{1}{2}m\omega^2 x^2. \tag{2.9}$$

In the formalism of quantum mechanics, the classical variables of position and momentum become operators. Mathematically, operators act upon quantum states and reveal information regarding a system. In general, operators act as measurements for a quantum system. For example, if the state of the spring in the example above is defined as $|\psi\rangle$, we would apply the position operator, $\hat{x}$ to the state in order to calculate the position of the mass. Similarly, if we act the momentum operator, $\hat{p}$ on the state, the result is the momentum of the state.

Although this change to the quantum regime seems straightforward, there is a very important caveat with regards to quantum operators. In quantum mechanics, it is not possible to measure with certainty the value of two conjugate variables for a system. Conjugate variables are properties of a system connected through the Lagrangian for the system, which is a description of the behavior of the system. This is in stark contrast to measurements in classical mechanics. In principle, it is possible to measure with absolute certainty the value of the momentum and position for a classical object.

Heisenberg showed that for the uncertainty in measuring position and momentum of a quantum state must be larger than Planck's constant by two

$$\sigma_x \sigma_p \geq \frac{\hbar}{2}. \tag{2.10}$$

A generalized form of this relation holds for any pair of non-commuting operators, or operators that do not satisfy the commutation relation [41]

$$\left[\hat{A}, \hat{B}\right] \equiv \hat{A}\hat{B} - \hat{B}\hat{A} = 0. \tag{2.11}$$

Classically conjugate variables become non-commuting quantum operators. Philosophically, non-commuting operators are related in that applying one to the system inherently changes the system and thus measurement of the second one will be affected by the first measurement. This is one of the philosophical cruxes of quantum mechanics. Physical systems are unknown to an observer and in order to gain information of the system, measurements must be made, but the measurements inherently interact with the system and irreversibly change the system. As a result, it is impossible to know with complete certainty the values of two non-commuting operators, such as position and momentum.

To move to the quantum regime, the position and momentum in the Hamiltonian from Eq. 2.9 become operators. Let us define two operators, $\hat{a}$ and $\hat{a}^\dagger$ in terms of $\hat{x}$ and $\hat{p}$ [42]

$$\hat{a} = \sqrt{\frac{m\omega}{2\hbar}}\left(\hat{x} + \frac{i\hat{p}}{m\omega}\right) \tag{2.12}$$

$$\hat{a}^\dagger = \sqrt{\frac{m\omega}{2\hbar}}\left(\hat{x} - \frac{i\hat{p}}{m\omega}\right), \tag{2.13}$$

which have a commutation relation of $\left[\hat{a}, \hat{a}^\dagger\right] = 1$. The operator $\hat{a}^\dagger$ is the Hermitian conjugate of $\hat{a}$. $\hat{a}^\dagger$ is known as the creation operator while $\hat{a}$ is the annihilation operator. The names for these operator result from the action each operator has on the quantum harmonic oscillator. The creation operator raises the quantum state

from one energy level to the next. The annihilation operator lowers the state by one energy level. We can also define two operators that are related to the position and momentum operators, called the quadrature operators [43],

$$\hat{X} = \sqrt{\frac{m\omega}{\hbar}}\hat{x} = \frac{1}{2}\left(\hat{a}^\dagger + \hat{a}\right) \tag{2.14}$$

$$\hat{Y} = \sqrt{\frac{1}{2m\hbar\omega}}\hat{x} = \frac{1}{2}\left(\hat{a}^\dagger - \hat{a}\right). \tag{2.15}$$

The creation and annihilation operators can be combined to create the number operator

$$\hat{N} = \hat{a}^\dagger\hat{a}. \tag{2.16}$$

When acting on a state of the quantum harmonic oscillator, the number operator returns the energy level in which the state resides. By inserting Eqs. 2.12 and 2.13 into the Eq. 2.9, we can reformulate the Hamiltonian in terms of the creation and annihilation operator to reveal a simple and meaningful form

$$\hat{\mathcal{H}} = \hbar\omega\left(\hat{a}^\dagger\hat{a} + \frac{1}{2}\right) = \hbar\omega\left(\hat{N} + \frac{1}{2}\right). \tag{2.17}$$

In Dirac notation, states of the quantum harmonic oscillator are written as

$$|\psi\rangle = |n\rangle, \tag{2.18}$$

where n is the energy level of the quantum oscillator and required to be a positive integer. This state is the eigenstate of the number operator, $\hat{N}$, with an eigenvalue equal to the level of the oscillator. The eigenvalues for the creation and annihilation

operators are defined as

$$\hat{a}\,|n\rangle = \sqrt{n}\,|n-1\rangle \tag{2.19}$$

$$\hat{a}^{\dagger}\,|n\rangle = \sqrt{n+1}\,|n+1\rangle\,. \tag{2.20}$$

To find the energy of a state, we apply the Hamiltonian

$$\hat{\mathcal{H}}\,|n\rangle = \hbar\omega\left(\hat{N}+\frac{1}{2}\right)|n\rangle = \hbar\omega\left(n+\frac{1}{2}\right)|n\rangle\,. \tag{2.21}$$

Therefore the energy of the quantum harmonic oscillator is easily extracted from Eq. 2.21

$$E_n = \hbar\omega\left(n+\frac{1}{2}\right). \tag{2.22}$$

It is clear that for the ground state, $|\psi\rangle = |0\rangle$, the energy is $E_0 = \frac{1}{2}\hbar\omega$. Even at the lowest energy, the state has a nonzero energy. This is the zero-point energy of the oscillator, in contrast with the classical harmonic oscillator.

For the classical harmonic oscillator, the oscillation energy is allowed to be continuous. However, in the quantum harmonic oscillator, the energy values that are allowed become quantized. The quantization of the energy is performed by restricting the oscillation frequency to be discrete values. The allowed energy levels from the example above are odd-integer multiples of $\hbar\omega/2$.

The derivation for a quantum oscillator is a brief example of the difference in formalism between the classical and quantum regimes. An important result of examining the quantum harmonic oscillator is the derivation of the creation and annihilation operators. Familiarity with these operators allows one to extend

the formalism to quantum optics easily. As we will see in the next section, $\hat{a}$ and $\hat{a}^\dagger$ are also used with the electric field in the number basis. In order to see this correspondence, we must first quantize the electric field.

2.2. Quantization of the Electric Field

In general, light is governed by Maxwell's equations, a set of four equations that describe the behavior of electric and magnetic fields. In free space without charges, Maxwell's equations are

$$\nabla \cdot \mathbf{E} = 0 \tag{2.23}$$

$$\nabla \cdot \mathbf{B} = 0 \tag{2.24}$$

$$\nabla \times \mathbf{E} = \frac{-\partial \mathbf{B}}{\partial t} \tag{2.25}$$

$$\nabla \times \mathbf{B} = \mu_0 \epsilon_0 \frac{\partial \mathbf{E}}{\partial t}, \tag{2.26}$$

where $\mathbf{E}$ is the electric field, $\mathbf{B}$ is the magnetic field, μ_0 is the permeability of free space, and ϵ_0 is the permittivity of free space.

By taking the curl of Eq. 2.25, inserting Eq. 2.26 and using a vector identity[2], the wave equation can be derived

$$\nabla^2 \mathbf{E} - \mu_0 \epsilon_0 \frac{\partial^2 \mathbf{E}}{\partial t^2} = 0. \tag{2.27}$$

The wave equation describes how the electric field travels through space and time by relating the second derivatives of these coordinates. The derivatives are related by a constant, $\mu_0 \epsilon_0$, which together is also a fundamental constant, c, the speed of

[2]The identity is $\nabla \times \nabla \times \mathbf{E} = \nabla (\nabla \cdot \mathbf{E}) - \nabla^2 \mathbf{E}$, where ∇^2 is the Laplacian

the light

$$\mu_0 \epsilon_0 = \frac{1}{c^2}. \tag{2.28}$$

It is convenient to describe the electric and magnetic fields in terms of a vector potential, $\mathbf{A}$

$$\mathbf{B} = \nabla \times \mathbf{A} \tag{2.29}$$

$$\mathbf{E} = -\frac{\partial \mathbf{A}}{\partial t}. \tag{2.30}$$

The vector potential also satisfies the wave equation

$$\nabla^2 \mathbf{A} - \mu_0 \epsilon_0 \frac{\partial^2 \mathbf{A}}{\partial t^2} = 0. \tag{2.31}$$

With the vector potential, the form of the equations are easier to transform into quantum mechanical equations by replacing the vector potential with quantum operators.

To make sense of these equations, we will consider the fields in a cube with each side of length L. Then the solutions to this wave equation are a sum of the contributions of all the modes within a cavity over an expansion of plane waves [43]

$$\mathbf{A}(\mathbf{r}, t) = \sum_{\mathbf{k}} \sum_{\xi=1,2} \mathbf{e}_{\mathbf{k}\xi} \left\{ A_{\mathbf{k}\xi} \exp\left[i(\mathbf{k} \cdot \mathbf{r} - \omega_k t)\right] + A^*_{\mathbf{k}\xi} \exp\left[-i(\mathbf{k} \cdot \mathbf{r} - \omega_k t)\right] \right\}, \tag{2.32}$$

where $A_{\mathbf{k}\xi}$ are constants that determine the strength of the contribution from each mode, $\mathbf{k}$ is the wavevector, ξ are the transverse spatial polarization, and $\mathbf{e}_{\mathbf{k}\xi}$ is a unit vector in the direction of the polarization of the mode. The wavevector has a

component in each spatial direction and the allowed values are integers

$$k_j = \frac{2\pi\nu_j}{L}. \tag{2.33}$$

The index j is over the spatial dimensions, $j = x, y, z$ and ν_j is a positive integer (including zero) denoting the mode number. The polarization vectors are transverse by definition and chosen to be perpendicular such that

$$\mathbf{e}_{\mathbf{k}\xi} \cdot \mathbf{e}_{\mathbf{k}\xi'} = \delta_{\xi\xi'}. \tag{2.34}$$

Now that we have a full solution for the vector potential in the cube, we can derive the electric field using Eq. 2.30,

$$\mathbf{E}(\mathbf{r}, t) = \sum_{\mathbf{k}} \sum_{\xi=1,2} \mathbf{e}_{\mathbf{k}\xi} i\omega_k \left\{ A_{\mathbf{k}\xi} \exp\left[i(\mathbf{k}\cdot\mathbf{r} - \omega_k t)\right] + A^*_{\mathbf{k}\xi} \exp\left[-i(\mathbf{k}\cdot\mathbf{r} - \omega_k t)\right] \right\}. \tag{2.35}$$

The magnetic field is obtained similarly from Eq. 2.29,

$$\mathbf{B}(\mathbf{r}, t) = \sum_{\mathbf{k}} \sum_{\xi=1,2} \frac{\mathbf{k} \times \mathbf{e}_{\mathbf{k}\xi}}{k} ik \left\{ A_{\mathbf{k}\xi} \exp\left[i(\mathbf{k}\cdot\mathbf{r} - \omega_k t)\right] + A^*_{\mathbf{k}\xi} \exp\left[-i(\mathbf{k}\cdot\mathbf{r} - \omega_k t)\right] \right\}. \tag{2.36}$$

As expected, dividing $\mathbf{E}$ by $\mathbf{B}$ recovers the speed of light through the definition $\omega = ck$. With equations for the electric and magnetic field, we can find the total energy in the cavity

$$\mathcal{E} = \frac{1}{2} \int_{\text{cavity}} dV \left[\epsilon_0 \mathbf{E}(\mathbf{r}, t) \cdot \mathbf{E}(\mathbf{r}, t) + \frac{1}{\mu_0} \mathbf{B}(\mathbf{r}, t) \cdot \mathbf{B}(\mathbf{r}, t) \right]. \tag{2.37}$$

The dot products of the electric and magnetic fields result in a Kronecker delta function from the exponential terms

$$\int_{\text{cavity}} dV \, exp\left[\pm i \left(\mathbf{k} - \mathbf{k}'\right) \cdot \mathbf{r}\right] = V \delta_{\mathbf{k},\mathbf{k}'}, \tag{2.38}$$

where $V = L^3$ is the volume of the cube. After some algebra and invoking the orthogonality of the mode functions, the total energy in the cube cavity becomes

$$\mathcal{E} = \sum_{\mathbf{k}} \sum_{\xi} \epsilon_0 V \omega_k^2 \left(A_{\mathbf{k}\xi} A_{\mathbf{k}\xi}^* + A_{\mathbf{k}\xi}^* A_{\mathbf{k}\xi} \right). \tag{2.39}$$

Classically, the terms in the parentheses can be combined together. However, in the quantum formalism, it is important to preserve the order of the fields, as not all variables commute as discussed in the previous section.

To complete the quantization of the electric field, we must turn the mode functions into quantum operators. The mode functions now become operators that create or annihilate photons in the chosen mode. Then modifying the creation and annihilation operators to have a mode specific index

$$\hat{a}_{\mathbf{k}\xi} \left| n_{\mathbf{k}\xi} \right\rangle = \sqrt{n_{\mathbf{k}\xi}} \left| n_{\mathbf{k}\xi} - 1 \right\rangle \tag{2.40}$$

$$\hat{a}_{\mathbf{k}\xi}^{\dagger} \left| n_{\mathbf{k}\xi} \right\rangle = \sqrt{n_{\mathbf{k}\xi} + 1} \left| n_{\mathbf{k}\xi} + 1 \right\rangle. \tag{2.41}$$

Comparing Eq. 2.21 and Eq. 2.39 and noting that $\hat{a}\hat{a}^\dagger = 1 + \hat{a}^\dagger\hat{a}$, the form of the mode amplitudes as a quantum operator can be found by inspection

$$A_{\mathbf{k}\xi} \rightarrow \sqrt{\frac{\hbar}{2\epsilon_0 V\omega_k}}\hat{a}_{\mathbf{k}\xi} \tag{2.42}$$

$$A^*_{\mathbf{k}\xi} \rightarrow \sqrt{\frac{\hbar}{2\epsilon_0 V\omega_k}}\hat{a}^\dagger_{\mathbf{k}\xi}. \tag{2.43}$$

For a given mode, the full electric field operator is then

$$\hat{E}_{\mathbf{k}\xi} = \mathbf{e}_{\mathbf{k}\xi}\sqrt{\frac{\hbar\omega_k}{2\epsilon_0 V}}\left\{\hat{a}_{\mathbf{k}\xi}exp[i(\mathbf{k}\cdot\mathbf{r} - \omega_k t)] + \hat{a}^\dagger_{\mathbf{k}\xi}exp[-i(\mathbf{k}\cdot\mathbf{r} - \omega_k t)]\right\}. \tag{2.44}$$

2.3. Number, Coherent, and Thermal States of Light

The eigenstates of the creation and number operators, $|n_{\mathbf{k}\xi}\rangle$ are also called Fock states. By definition, Fock states are excitations of a single mode. Any Fock state can be written as a product of creation operators

$$|n_k\rangle = \frac{\left(\hat{a}^\dagger_k\right)^n}{n_k!^{1/2}}|0\rangle. \tag{2.45}$$

Fock states are orthogonal ($\langle m|n\rangle = \delta_{nm}$) and comprise a complete basis of Hilbert space. The completeness relation is

$$\sum_{n_k=0}^{\infty}|n_k\rangle\langle n_k| = \mathbb{1}. \tag{2.46}$$

Fock states are a common basis for decomposing fields in quantum optics with an intuitive meaning. The value n_k is the number of excitations of the electric field, or loosely the number of photons in a given mode, k. If the excitations of the electric field are not in a single mode, but over multiple modes with a total number of

photons, then the state is no longer a Fock state. The state is a number state. Number states can occupy multiple modes, but with a total number of photons over all the modes used to define the number state. In this case, the state can be written as a product over the modes

$$|\Psi_n\rangle = \prod_m c_{n,m} |n_m\rangle \,, \tag{2.47}$$

where the coefficients $c_{n,m}$ define the probability amplitude to detect the photon number state in a specific mode, indexed by m. Then the state can be defined as a sum over the number basis

$$|\Psi\rangle = \sum_n |\Psi_n\rangle = \sum_n \prod_m c_{n,m} |n_m\rangle \,. \tag{2.48}$$

With a description of the Fock basis, we can properly describe a common state called the coherent state. The coherent state of light is a state that has a constant relation between the phase of the states that comprise the basis. An important example of a coherent state is the light produced by a laser. Coherent light is an especially interesting example of light since it has classical behavior that can be adequately described by quantum theory.

A coherent state is typically denoted by the complex number, α. The coherent state, $|\alpha\rangle$, can be written as a sum of Fock states [44]

$$|\alpha\rangle = e^{-\frac{|\alpha|^2}{2}} \sum_{n=0}^{\infty} \frac{\alpha^n}{\sqrt{n!}} |n\rangle \,. \tag{2.49}$$

The expectation value and second moment of the number operator for a coherent state is

$$\langle n \rangle = \langle \alpha | \, \hat{n} \, | \alpha \rangle = \langle \alpha | \, \hat{a}^\dagger \hat{a} \, | \alpha \rangle = |\alpha|^2 \tag{2.50}$$

$$\left\langle n^2 \right\rangle = \langle \alpha | \, \hat{n}^2 \, | \alpha \rangle = |\alpha|^4 + |\alpha|^2. \tag{2.51}$$

The variance of the photon number for the coherent state is found by using Eq. 2.50 and Eq. 2.51:

$$(\Delta n)^2 \equiv \left\langle n^2 \right\rangle - \langle n \rangle^2 = |\alpha|^2 = \langle n \rangle \, . \tag{2.52}$$

As with conjugate variables of position and momentum, the uncertainty in measuring number is constrained by a measurement of the conjugate variable. For coherent states, it is easiest to examine the uncertainty relation between the quadratures X and Y, as defined in Eq. 2.14 and Eq. 2.15.

By inserting the quadratures into Eq. 2.10, we arrive at the Heisenberg uncertainty relation for the quadratures of a field

$$(\Delta X)^2 (\Delta Y)^2 \geq \frac{1}{16}. \tag{2.53}$$

For a coherent state, the uncertainties of the quadratures are

$$(\Delta X)^2 = (\Delta Y)^2 = \frac{1}{4}. \tag{2.54}$$

By definition, a coherent state is the minimum-uncertainty state possible and is displaced from the vacuum state by α. The coherent state has an average number

of photons of $|\alpha|^2$. The quadratures can also be interpreted as the amplitude and phase of the field of the field. Thus, the amplitude and phase of the field are conjugate variables for light fields in the formalism of quantum mechanics.

The probability distributions of the states can be found by taking the inner product of a Fock state with the coherent state. For a coherent state, in a given mode the probability to find n photons in the mode is a Poisson distribution given by

$$P(n) = |\langle n|\alpha\rangle|^2 = e^{-|\alpha|^2}\frac{|\alpha|^{2n}}{n!} = e^{-\langle n\rangle}\frac{\langle n\rangle^n}{n!}. \tag{2.55}$$

For a Fock state, the probability to measure a particular photon number, n, in a given mode is somewhat trivial. If the state under measurement is a Fock state with a photon number different than n, then the value is zero by the orthogonality of the number state basis. If the state is a superposition of Fock states, or a number state, then the probability will pick out the probability for a given photon number

$$P(n) = |\langle n|\psi\rangle|^2 = \left|\langle n|\left(\sum_m c_{m,n}|n_m\rangle\right)\right|^2 = \sum_m |c_{m,n}|^2. \tag{2.56}$$

A state that has not yet been discussed is a thermal state of light. Thermal states created by blackbody radiation were the basis for Planck's original derivation to quantize the modes of a cavity that lead to quantum mechanics. The light radiates from the blackbody depending on the temperature in the form of a Boltzmann factor. From statistical mechanics, the probability that an oscillator

in thermal equilibrium is excited to the n state is given by [43]

$$P(n) = \frac{\exp\left[-\frac{E_n}{k_B T}\right]}{\sum_n \exp\left[-\frac{E_n}{k_B T}\right]}, \tag{2.57}$$

where k_B is the Boltzmann constant and the energy is the quantized energy of the harmonic oscillator, $E_n = n\hbar\omega$. With the substitution $U = \exp(\hbar\omega)$, Eq. 2.57 becomes

$$P(n) = \frac{U^n}{\sum_n U^n} = (1-U)U^n. \tag{2.58}$$

The denominator was changed by using the definition for a geometric series. We can further simplify this equation by looking at the expectation value for n. By using the definition of the expectation value and a little algebra, we find

$$\langle n \rangle = \sum_n nP(n) = \frac{U}{1-U} = \frac{1}{\exp(\hbar\omega/k_B T) - 1}. \tag{2.59}$$

And by solving for U in Eq. 2.59, we can rewrite the probability purely in terms of the mean number

$$P(n) = \frac{1}{1+\langle n \rangle}\left(\frac{\langle n \rangle}{1+\langle n \rangle}\right)^n. \tag{2.60}$$

By comparing the three distributions for a coherent state, a number state, and a thermal state, it is clear that the measured distributions would be quite different. For example, for a mean number of 2, the three distributions are plotted in Fig. 2.2. As we will discuss in the following section, the difference in the

statistics of these states drastically affects the coherence measurements of the states and is often utilized to determine the type of light being measured.

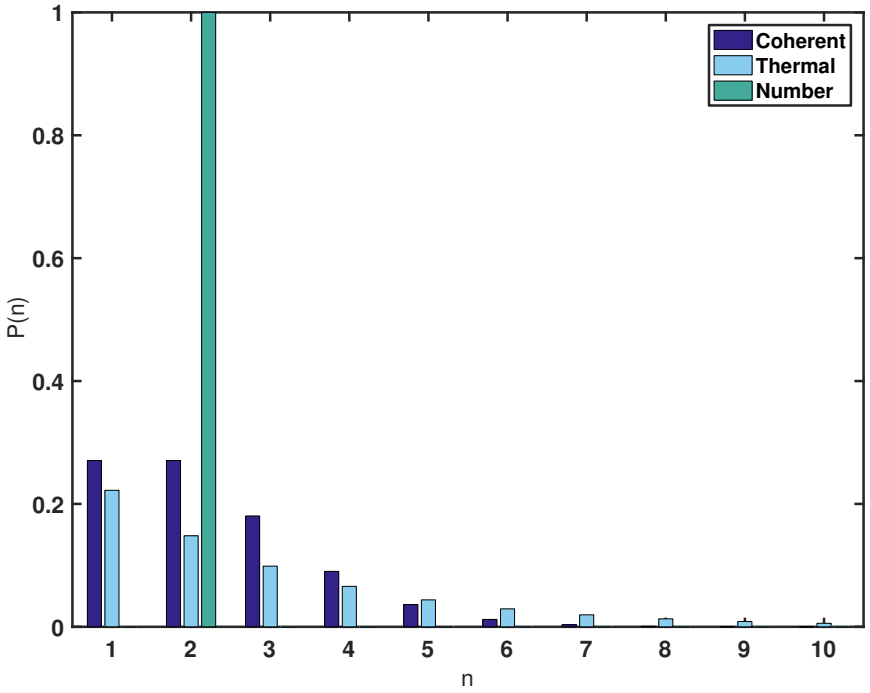

FIGURE 2.2. Depiction of difference in the photon number distributions expected for coherent, number, and thermal states of light with $\langle n \rangle = 2$.

It should be noted that often attenuators are used with a laser to decrease the intensity of the laser light to the level of single photons to perform experiments in quantum optics. However, although an attenuated laser may have an intensity on the order of a single photon, the statistics of the light continue to follow a Poisson distribution, with a much lower $\langle n \rangle$. This is not the same as using a true number state, created via a process such as spontaneous parametric down conversion.

2.4. Coherence Measurements

Many of the effects of optics, both classical and quantum, result from the coherence properties of light. From interference of different beams of light,

interactions between matter and light, coherence plays a key role in these phenomena. An important measurement in quantum optics is the coherence of the field.

The first order coherence is a measure of the temporal stability of an electric field, $E(t)$, and for stationary fields is defined as [45]

$$g^{(1)}(\tau) = \frac{\langle E^*(t)E(t+\tau)\rangle}{\langle |E(t)|^2\rangle}, \tag{2.61}$$

where the angled brackets denote time averaging over t. When the first-order coherence is measured between two fields, it quantifies the amount to which both fields are stationary and able to interfere or interact. If the two fields are first-order coherent, there will be interference and the two fields will effectively interact and produce visible fringes.

The numerator in Eq. 2.61 is similar to the intensity of the field, $I(t) = \langle E^*(t)E(t)\rangle$. From the first-order coherence, another useful parameter is the visibility of the interference. Physically, the visibility is the depth of the fringes and defined as:

$$\text{Visibility} = \frac{I(t)_{\max} - I(t)_{\min}}{I(t)_{\max} + I(t)_{\min}}. \tag{2.62}$$

Both the visibility and the first-order coherence are bound to be in the range $[0, 1]$. It is clear that first-order coherence is an interaction between the fields of two beams of light. However, in quantum optics experiments, the second-order coherence is typically of more interest. A simple explanation involves the Fock state described in the previous section. A Fock state with well defined number will have

a random phase, causing the interference with any other field to be random, and appear to look the same as thermal light which also has a random phase.

The second-order coherence function is a measure of the second-order product of the field, or the intensity. The second-order coherence function for classical fields is defined as

$$g^{(2)}(\mathbf{r}_1, \mathbf{r}_2, \tau) = \frac{\langle \mathbf{E}^*(\mathbf{r}_1, t)\mathbf{E}^*(\mathbf{r}_2, t+\tau)\mathbf{E}(\mathbf{r}_2, t+\tau)\mathbf{E}(\mathbf{r}_1, t)\rangle}{\langle \mathbf{E}^*(\mathbf{r}_1, t)\mathbf{E}(\mathbf{r}_1, t)\rangle \langle \mathbf{E}^*(\mathbf{r}_2, t+\tau)\mathbf{E}(\mathbf{r}_2, t+\tau)\rangle}, \tag{2.63}$$

where $\mathbf{r}_1, \mathbf{r}_2$ are two locations of the beams. If the beams are stationary, the equation further simplifies:

$$g^{(2)}(\tau) = \frac{\langle I(t)I(t+\tau)\rangle}{\langle I(t)\rangle \langle I(t+\tau)\rangle}. \tag{2.64}$$

Again, this is for classical fields. The second-order coherence function for quantum states modifies Eq. 2.64 by changing the fields to quantum operators. The second-order correlation function simplifies to the form [43]

$$g^{(2)}(\tau) = \frac{\left\langle \hat{a}^\dagger \hat{a}^\dagger \hat{a}\hat{a} \right\rangle}{\left\langle \hat{a}^\dagger \hat{a} \right\rangle^2} = \frac{\langle n(n-1)\rangle}{\langle n\rangle^2} = \frac{\langle n^2\rangle - \langle n\rangle}{\langle n\rangle^2} = 1 + \frac{(\Delta n)^2 - \langle n\rangle}{\langle n\rangle^2}. \tag{2.65}$$

By definition, the variance $(\Delta n)^2$ must be non-negative. For a number state, where the variance is 0, the second-order coherence for fields with $\langle n\rangle \geq 1$ is

$$g^{(2)}(\tau) = 1 - \frac{1}{\langle n\rangle}, \tag{2.66}$$

which is inherently non-classical if $\tau = 0$. To see this, we must examine the second-order coherence function for classic fields, Eq. 2.64 with $\tau = 0$. From the Cauchy-Schwartz inequality, $\langle I\rangle^2 \leq \langle I^2\rangle$. Therefore the numerator must always be less than

the denominator, causing $g^{(2)}(0)$ to have a minimum value of one without an upper bound. For a number state with an average photon number of any value greater than 0, $g^{(2)}(0)$ will be less than one. This is a violation of the Cauchy-Schwartz inequality and signature of a non-classical state. Table 2.1 shows the values for the states described in the previous section. The second-order coherence function shows a distinct difference between the statistical nature of each of the states.

TABLE 2.1. Second-order coherence function values

State	$g^{(2)}(\tau = 0)$
Coherent	$g^{(2)}(0) = 1$
Thermal	$g^{(2)}(0) = 2$
Number	$g^{(2)}(0) = 1 - \frac{1}{\langle n \rangle}$

For a perfect single-photon state, the second-order coherence function will be exactly 0. Indeed, a second-order coherence function measurement is typically used to show a state is non-classical and even that the field is specifically a single-photon state.

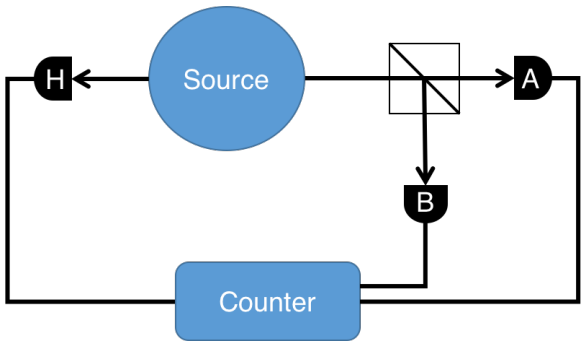

FIGURE 2.3. Schematic of detection setup for measuring second-order coherence function. In the experiment performed by Grangier *et al.*, the source was a cascade atom source producing pairs. One photon went to detector H and one photon went to the beamsplitter that sent the other photon to A or B.

Experimentally, the second-order coherence is typically measured by counting photons on highly sensitive detectors on the output of a beamsplitter. This

detector setup is called a Hanbury-Brown Twiss setup, in honor of the experiment conducted by Hanbury-Brown and Twiss in 1956 to measure the correlations from distant stars at two different radio detectors [5]. One of the earliest second-order coherence function measurements was made by Grangier, Roger, and Aspect in 1985 where they measured a highly nonclassical value for quantum states emitted by an atom [9]. To calculate the second-order coherence function, the number of clicks are recorded by two detectors, labeled A and B in Fig. 2.3. In the original experiment, the detectors A and B were gated depending on the herald detector, H. The second-order coherence measurement is calculated as follows [46]

$$g^{(2)}(\tau = 0) = \frac{N_{HAB} N_H}{N_{HA} N_{HB}}. \tag{2.67}$$

The subscripts in Eq. 2.67 pertain to the detectors that are being recorded. For example, during a given time window, N_H is the number of counts recorded by detector A, N_{HA} is the number of coincidence detections between detectors H and A, and N_{HAB} is the number of triple coincidences between all three detectors during the time window.

When the purpose is to show that a state is inherently quantum in nature by violating the classical bound for the second-order coherence measurement, this experimental technique is adequate. However, if the purpose is to determine the photon number probability distribution, the second-order coherence is not sufficient. In this case, it is important to measure the photon number distribution, which requires a more sophisticated measurement, such as using multiplexed detectors for direct inversion. This method will be discussed in Chapter IV.

CHAPTER III

OPTICAL FIBERS

At the heart of communications of the modern world sit optical fibers, sending along information close to the speed of light in vacuum all over the world. Optical fibers are like pipes for light, efficiently containing light through the length of the fiber. Fibers are truly modern wonders, even leading to a Nobel Prize in 2009 for Charles Kao for his work on the development of the silica optical waveguide along with George Hockham [26]. After decades of development, optical fibers that are extremely high in quality are readably available at low cost and have revolutionized many industries.

Optical fibers have been fabricated with very small cores and good waveguiding, giving rise to high energy density for easily achievable laser pulses. The use of optical fibers has opened a large variety of applications of nonlinear optics that have propelled experimental results in quantum optics. In this chapter, we will cover the basics of fiber optics before moving into the nonlinear behavior of light within optical fibers. The creation of quantum states of light in optical fibers and quantum frequency translation will be discussed.

3.1. Basics of Optical Fibers

Optical fibers are commonly composed of glass and utilize the phenomena of total internal reflection.[1] When light is incident upon an interface between two different materials, the light will mostly transmit through the interface at a

[1]There are other types of fibers that use other methods to produce waveguiding such as photonic bandgap fibers, but these fibers will not be discussed in this dissertation.

shifted angle that depends on the ratio of the index of refraction of the light in the materials. This gives rise to the bending that light rays exhibit in different materials, which is utilized for the creation of lenses. However, if the angle of incidence is large enough, larger than the critical angle, an interesting phenomena occurs: the light does not transmit through the interface, but rather is reflected off the surface at the same angle! This is total internal reflection (TIR) and an important technique for guiding light through optical fibers.[2]

The typical structure for optical fibers is a cylinder with a core glass and a shell of glass around the core. The core glass has a higher index of refraction than the cladding. These types of fibers are called step-index fibers because of the abrupt change in the index of refraction at the boundary between the two glasses. The index contrast is commonly achieved by either doping the core glass with elements that have a higher index (up-doping) or doping the cladding glass with elements that have a lower index of refraction than the core (down-doping). An example of the index of refraction profile between the core and cladding are shown in Fig. 3.1.

Since the critical angle depends on the index of refraction of the core and the cladding, the cone of allowed angles for light to enter depends on the two indices as well. The cone of accepted angles is also called the numerical aperture (NA) and is defined as:

$$\mathrm{NA} = \sqrt{n_{\mathrm{core}}^2 - n_{\mathrm{cladding}}^2} \tag{3.1}$$

[2]A practical example of this can be demonstrated by going to the bottom of a swimming pool and looking up at the surface. By looking off in the distance, there will be a point when you can no longer see out of the pool, but instead see the reflections off the bottom and sides. This is because light that reflected off those surfaces is reflected from the interface, undergoing TIR.

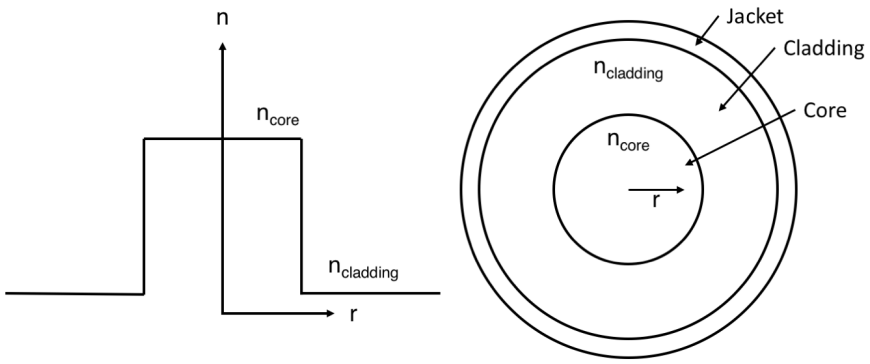

FIGURE 3.1. Left: Profile of the index of refraction along the radial direction for a typical step index fiber. The index of refraction of the core is higher than the cladding to allow for total internal reflection. Right: Head on view of a standard step index profile. The core is in the center, surrounded by a cladding. The outer most edge is a protective jacket and does not affect the waveguiding in the core of the fiber.

With the NA, a normalized frequency can be defined, denoted as the V parameter. The V parameter is an estimate for the number of spatial transverse modes that are able to propagate through the fiber. The V parameter is a useful tool for estimating the number of fiber modes with the cutoff for single-mode operation at values lower than $V = 2.405$. The V parameter is defined as [47]

$$V = \frac{2\pi a_0}{\lambda}\mathrm{NA} = \frac{2\pi a_0}{\lambda}\sqrt{n_{\mathrm{core}}^2 - n_{\mathrm{cladding}}^2}, \tag{3.2}$$

where a_0 is the radius of the fiber core and λ is the wavelength of the light in vacuum. Fibers that are designed to only allow for frequencies below the single-mode limit for the V parameter are called single mode fibers and are common for optical transmission lines. The V parameter arises from solving the boundary conditions for a cylindrical waveguide, which produces Bessel functions for the modes of the light in the optical fiber [48].

Light travels along the fiber and is mostly confined to the core. In the paraxial limit, light travels along the z-axis of the fiber with $\hat{k} \parallel \hat{z}$. Then the momentum of the light has a magnitude equal to the propagation constant of the fiber:

$$\vec{k} = k_z \hat{z} = \beta \hat{z} = \frac{n(\omega)\omega}{c} \hat{z}. \tag{3.3}$$

The propagation constant is defined by three terms: the material dispersion, waveguide dispersion, and nonlinear dispersion. The material dispersion is determined by the material properties of the optical fiber, while the waveguide dispersion is determined by the geometry. Material dispersion is typically much larger than waveguide dispersion, with the exception of wavelengths close to the zero dispersion wavelength [47]. In addition to the fiber core and the material properties, the nonlinear dispersion depends on the intensity of the light.

For fibers that are cylindrically symmetric, there is coupling between the two polarization axes of the fiber. Some fibers have been designed that break the symmetry in the index of refraction by including additional material of a higher index of refraction along one polarization axis. This creates a birefringence that the optical modes experience and hence these fibers are called birefringent fibers. One type of birefringent fiber is a PANDA type, with two circular rods placed along the slow axis of the fiber. Fiber birefringence results in a linear offset to the dispersion for light polarized along the slow axis. In breaking the symmetry, the two polarization modes become decoupled and the light traveling along one polarization through the fiber will stay oriented along that polarization. A schematic of a PANDA fiber is shown in Fig. 3.2.

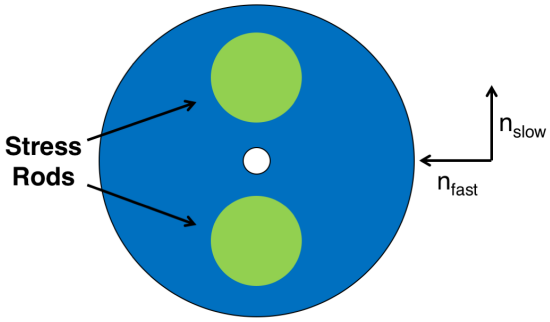

FIGURE 3.2. A schematic of a typical PANDA type birefringent fiber showing the presence of rods along one axis. This axis is called the slow axis since the index of refraction is larger along this axis resulting from the rods. This results in a linear addition to the dispersion for light polarized along this axis.

The first derivative of the propagation constant with respect to frequency is the inverse group velocity, which we will call the *group slowness* for ease. Positive group slowness values correspond to frequency ranges were the material exhibits normal dispersion, where the index of refraction increases with increasing frequency. Anomalous dispersion occurs at frequencies where the group slowness is negative, or the index of refraction increases with decreasing frequency.

The second derivative of the propagation constant is called the group velocity dispersion (GVD). GVD describes the rate at which the group slowness changes with frequency. GVD is an important parameter in describing the propagation of pulses of light, where there are many frequency components and differences in propagation speeds for the components will change the temporal shape of the original pulse.

In optical fibers, the GVD is modified slightly to define the dispersion parameter, D. The D parameter is in units of (ps/(nm·km)) and is related to the

second derivative of the propagation constant with respect to frequency by

$$D = -\frac{\omega^2}{2\pi c} GVD = -\frac{\omega^2}{2\pi c}\left(\frac{d^2\beta}{d\omega^2}\right). \tag{3.4}$$

There is a special wavelength at which the dispersion due to the material and waveguide dispersion cancel out, which is called the zero dispersion wavelength (ZDW) [48]. At the ZDW, $D = 0$. The ZDW is in the infrared, around $\lambda_{ZDW} =$ 1300 nm for typical step index fibers. In addition to the presence of the ZDW, absorption from silica in the infrared is low. As result the extensive work has been done in source development at wavelengths in this range for the transmission of optical signals.

In typical step index fibers described above, the difference in the index of refraction between the core and the cladding is very small, less than a few percent of $n \approx 1.5$. Two decades ago, Philip Russell and colleagues pioneered a method to push the effective index of refraction of the cladding much closer to that of air, 1, by creating a photonic crystal fiber (PCF). The PCF has a core made of solid silica, but rather than having another type of glass as the cladding, the cladding is composed of a honeycomb structure with alternating silica and air [49]. The effective index of the cladding is a weighted average of the amount of air that occupies the cladding. As a result, the dispersion profile in a PCF is drastically different. In addition to the ZDW in the infrared, there is a second ZDW in the visible wavelength range that depends on the air filling fraction of the cladding [50]. Typical dispersion curves for a step index fiber and a PCF are shown below in Fig. 3.3 Having a ZDW in the visible opens the possibility for exploring a variety of nonlinear interactions in optical fibers at visible wavelengths. As we will discuss in the following sections, the linear behavior of the dispersion close to the ZDW allows

energy and momentum to be conserved for fields symmetrically spaced from the ZDW.

PCFs are typically considered "endlessly single-mode" fibers due to the nature of the structure in the cladding. Specifically, the photonic crystal nature of the cladding, hence the namesake, is what causes the V parameter to be modified such that all guided wavelengths will be below the single mode cutoff [51]. The ratio of the size of the individual air holes and the spacing between holes in the cladding changes the V parameter and is ultimately chosen to produce single mode operation for all guided wavelengths [52]. PCFs can be analyzed as step index fibers with the cladding index of refraction as a weighted average,

$$n_{\text{cladding}}(\omega) = f n_{\text{air}} + (1-f) n_{\text{core}}(\omega) = f + (1-f) n_{\text{core}}(\omega), \tag{3.5}$$

where f is the fraction of the cladding composed of air. This approximation is valid for a wide range of air-filling fractions, between $10\% - 90\%$ [53]. In addition to the air-filling fraction, the core diameter has a large effect on the dispersion properties of PCFs. Furthermore, the core diameters of PCFs are typically of the order 1μm, which is smaller than commercial single mode fibers, which are on the order of 10μm. This results in a larger nonlinear response in PCFs, which has been utilized to create very bright photon sources [35], as will be discussed in more detail below.

3.2. Nonlinear Wave Equation

In general, light is governed by fundamental equations labeled Maxwell's equations, originally formulated by James Clerk Maxwell and refined by Oliver Heaviside. There are a few exceptions where light is not well described by

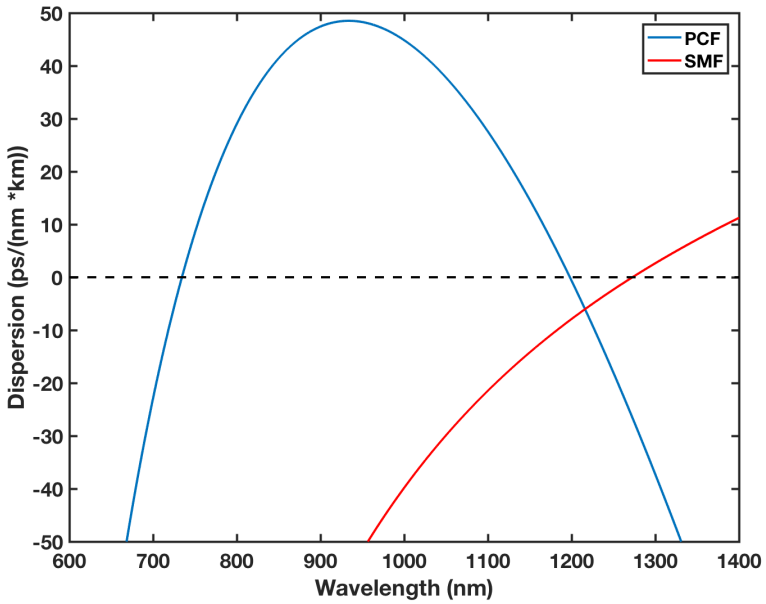

FIGURE 3.3. The dispersion curves of a photonic crystal fiber (blue) and a single mode, step index fiber (red, labeled SMF). Zero dispersion wavelengths (ZDW) occur when the dispersion curves are zero. The large contrast in the index of refraction between the core and the cladding for the PCF pulls the dispersion curve down in the visible region, producing a ZDW in the visible.

Maxwell's equations, but we will restrict ourselves to scenarios where the correction to Maxwell's equations are negligible. In a medium, Maxwell's equations are [54]

$$\nabla \cdot \mathbf{D} = \rho \tag{3.6}$$

$$\nabla \cdot \mathbf{B} = 0 \tag{3.7}$$

$$\nabla \times \mathbf{E} = \frac{-\partial \mathbf{B}}{\partial t} \tag{3.8}$$

$$\nabla \times \mathbf{H} = \frac{\partial \mathbf{D}}{\partial t} + \mathbf{J}, \tag{3.9}$$

where the bold letters denote vector quantities. The vacuum electric field is denoted by $\mathbf{E}$ and $\mathbf{D}$ is the electric displacement field. It should be noted that $\mathbf{E}$

and **D** have different units. Similarly, the vacuum magnetic field is denoted by **B** and the magnetic field in a material is **H**, also called the macroscopic magnetic field. ρ is the charge and **J** is the current density in the medium. We will restrict this discussion to media which are without charge, causing ρ and **J** to go to zero. The optical fibers used here are a neutral medium, thus free of charge sources and appropriately described by this assumption. Furthermore, we assume the optical fiber will be nonmagnetic. Then the vacuum and macroscopic magnetic fields are proportional,

$$\mathbf{B} = \mu_0 \mathbf{H}, \tag{3.10}$$

where μ_0 is the vacuum permeability.

A similar relation for the macroscopic and vacuum electric fields can be shown with the constant of proportionality being the vacuum permittivity. However, for the electric fields, there is an additional term to account for the behavior of the medium. This term is the polarization **P** of the medium. The polarization is also a vector and is the response of the medium to the presence of light. The relation is

$$\mathbf{D} = \epsilon_0 \mathbf{E} + \mathbf{P}. \tag{3.11}$$

Although the behavior of the medium is dominated by the linear term, we do not restrict this derivation to first order in the polarization. It is interesting to note that the linear behavior is what allows for the frequency of light passing through

glass to remain unchanged, for example through a glass window pane or through glasses.[3]

Maxwell's equations can be solved in terms of the vacuum fields and the polarization of the medium using Eq. 3.10 and Eq. 3.11

$$\nabla \cdot \mathbf{E} = -\frac{1}{\epsilon_0}\nabla \cdot \mathbf{P} \tag{3.12}$$

$$\nabla \cdot \mathbf{B} = 0 \tag{3.13}$$

$$\nabla \times \mathbf{E} = \frac{-\partial \mathbf{B}}{\partial t} \tag{3.14}$$

$$\nabla \times \mathbf{B} = \mu_0\epsilon_0\frac{\partial \mathbf{E}}{\partial t} + \mu_0\frac{\partial \mathbf{P}}{\partial t}. \tag{3.15}$$

With Maxwell's equations in a medium, the wave equation for governing the behavior of the light is found by taking the curl of the electric field **E**. This is the same procedure as when solving for the wave equation in free space, but the presence of the polarization term changes the free space wave equation by including an additional term involving **P**. By taking the curl of **E** and invoking the typical vector identity, we are left with the Laplacian of the electric field

$$\nabla \times \nabla \times \mathbf{E} = \nabla\left(\nabla \cdot \mathbf{E}\right) - \nabla^2\mathbf{E} = -\nabla^2\mathbf{E}. \tag{3.16}$$

The curl of the curl of the electric field produces two terms; the first term is the change in the divergence of the electric field and the second the Laplacian of the field. If there is no source, then the first term is clearly zero in free space as a result of Maxwell's equations. However, in a medium this is not the case, as shown from

[3]Distortions of *images* where the location of different colors of light is different or the size changes is a result of the glass having an index dependent on wavelength, not changing the frequency of the light as it passes through the glass.

Eq. 3.12. We assume that the divergence is much smaller than the Laplacian of the electric field, and therefore Eq. 3.16 is reduced to the second term. Then the nonlinear wave equation becomes

$$\nabla^2\mathbf{E} - \frac{1}{c^2}\frac{\partial^2\mathbf{E}}{\partial t^2} = \frac{1}{\epsilon_0 c}\frac{\partial^2\mathbf{P}}{\partial t^2}. \tag{3.17}$$

This equation looks like the wave equation for a driven wave. Expanding the polarization brings nonlinear terms into the wave equation. For ease, we group the nonlinear terms together

$$\mathbf{P} = \mathbf{P}^{(1)} + \mathbf{P}^{(\mathrm{NL})}. \tag{3.18}$$

The nonlinear response of the medium causes a wealth of phenomena, strongly dependent upon the medium involved. The induced polarization of the medium is related to the incident electric field by the electric susceptibility, $\chi^{(i)}$, where i is the order. In general, $\chi^{(i)}$ is a tensor of rank $i + 1$. In centrosymmetric materials, where the unit cell appears unchanged through inversion symmetry, the even-order terms of the electric susceptibility vanish. Optical fibers are centrosymmetric and therefore, the lowest order nonlinear term is third-order. In all materials, a third-order electric susceptibility is present, however the second-order term dominates in non-centrosymmetric media. The relation between the electric field and the

polarization is

$$\mathbf{P}^{(1)}(\mathbf{r},t) = \epsilon_0 \int_{-\infty}^{t'} \chi^{(1)}(t-t') \cdot \mathbf{E}(\mathbf{r},t')\, dt' \tag{3.19}$$

$$\mathbf{P}^{(\mathrm{NL})}(\mathbf{r},t) = \epsilon_0 \int_{-\infty}^{t_1} dt_1 \int_{t_1}^{t_2} dt_2 \int_{t_2}^{t^3} dt_3 \tag{3.20}$$

$$\times\, \chi^{(3)}(t-t_1, t-t_2, t-t_3) \vdots \mathbf{E}(\mathbf{r},t_1)\mathbf{E}(\mathbf{r},t_2)\mathbf{E}(\mathbf{r},t_3). \tag{3.21}$$

The induced polarization is rather complicated due to the time ordering of the fields in the optical fiber. For optical pulses that are longer than 1 ps, it is appropriate to assume that the response of the medium is instantaneous, causing the integrals in Eq. 3.21 to be evaluated at time t

$$\mathbf{P}^{(\mathrm{NL})}(\mathbf{r},t) = \epsilon_0 \chi^{(3)} \mathbf{E}(\mathbf{r},t)\mathbf{E}(\mathbf{r},t)\mathbf{E}(\mathbf{r},t). \tag{3.22}$$

3.3. Nonlinear Index of Refraction

Then in the frequency domain, the linear polarization and the electric field can be combined by defining a frequency dependent dielectric constant

$$\epsilon(\omega) = 1 + \chi^{(1)}(\omega) + 3\chi^{(3)}|E|^2. \tag{3.23}$$

We can relate Eq. 3.23 to the index of refraction by introducing a correction that is nonlinear in the electric field

$$n' = n + n_2|E|^2, \tag{3.24}$$

where n_2 is the nonlinear index coefficient. In general, the same procedure can be performed for the optical loss by including a nonlinear loss term dependent upon $|E|^2$

$$\alpha' = \alpha + \alpha_2 |E|^2. \tag{3.25}$$

The dielectric constant is not restricted to be real, but is indeed complex if there is loss. However, the assumption of negligible optical loss holds here as well, allowing us to neglect α_2 and α'. Alternatively, it can be seen as the third-order susceptibility being purely real. Therefore the nonlinear index coefficient becomes [48]

$$n_2 = \frac{3}{8n}\chi^{(3)}. \tag{3.26}$$

The nonlinear change to the index of refraction is known as the optical Kerr effect and gives rise to a nonlinear phase that depends on the intensity of the incident light. The Kerr effect can lead to intensity induced self-focusing within a material and is a common method for inducing mode-locked behavior in titanium-sapphire lasers. Additionally, this is the origin of self-phase modulation for ultrashort pulses through propagation in nonlinear media. The nonlinear phase is not constant through the temporal duration of the pulse, affecting the spectrum of the pulse. Self-phase modulation was first observed in 1967 in CS_2 [55] and further studied extensively in optical fibers by Roger Stolen and Chinlon Lin [56]. It is important to note the accuracy to which experimental results matched theoretical predictions by Stolen and Lin. There was excellent agreement between theory and experiment, verifying the underlying intensity dependent phase modulation. With a nonlinear

refractive index, it is straightforward to see how the change in the index of refraction causes the phase of the field to change.

A typical plane wave is described by the following

$$\mathbf{E}(\mathbf{r},t) = \mathbf{U}(x,y)A(z,t)e^{i(\beta_j z - \omega_j t)} + c.c., \tag{3.27}$$

where β is the propagation constant for the field and defined as $\beta \equiv (n(\omega)\omega)/c$, $U(x,y)$ describes the transverse spatial profile of the field, and $A(z,t)$ is the slowly varying envelope of the field. If the envelope does not change much over a particular distance, then the phase accumulated over a distance L for a given frequency is

$$\phi(L) = \beta_j L = \frac{n(\omega_j)\omega_j}{c} = \phi_0 + \frac{n_2\,\omega|E|^2 L}{c}, \tag{3.28}$$

where ϕ_0 is the phase accumulated in a linear medium. It is clear that the additional phase accumulated depends on the intensity of the incident field. This is the result of a phase modulation from one field on itself, but there are also effects from the presence of another field, called cross-phase modulation (XPM). XPM is similar to Eq. 3.28, with an additional term for the second field. However, in this dissertation, both effects are small relative to the processes of interest and therefore neglected.

3.4. Four-Wave-Mixing Processes

From the form of Eq. 3.22, there are three electric field terms and one polarization term. From this one nonlinear polarization term, a wealth of interesting phenomena arise. A common inelastic scattering process in $\chi^{(3)}$ media is

Raman scattering, where a photon is absorbed by the medium, energy is transferred to a phonon in the medium, and a lower energy photon (called the Stokes photon) is transmitted. In contrast, the energy from a phonon can be added to the photon, creating a photon that is shifted to a higher energy, called an anti-Stokes photon. Raman scattering will be further discussed in later chapters as it is can negatively affect the desired creation of photon pairs.

Expanding the total electric field as a summation of four electric fields illuminates the complexity of terms arising from the nonlinear polarization term [48]. Explicitly, the total electric field is

$$\mathbf{E} = \frac{1}{2}\hat{x}\sum_{j=1}^{4} E_j e^{i(\beta_j z - \omega_j t)} + c.c., \tag{3.29}$$

where the sum over j denotes the different fields. We are assuming all the fields are copolarized in the $\hat{x}$ direction. The nonlinear polarization term can be expanded in a similar manner

$$\mathbf{P} = \frac{1}{2}\hat{x}\sum_{j=1}^{4} P_j e^{i(\beta_j z - \omega_j t)} + c.c. \tag{3.30}$$

By substituting Eq. 3.29 and Eq. 3.30 into Eq. 3.22, we can solve for the terms that involve four-wave mixing. Indeed, there are many terms in this equation, but we may neglect many of them. Terms corresponding to interactions between two fields (XPM) or one field with itself (SPM) are neglected as described previously. The remaining terms correspond to third harmonic generation, modulation instability, phase conjugation, and Bragg scattering.

Third harmonic generation is when three photons of frequency ω are absorbed by the fiber and create a photon at frequency 3ω. In practice, it is very challenging

to achieve third harmonic generation in optical fibers. Although energy is conserved in the process by definition, it is very challenging to conserve momentum in optical fibers due to the dispersion relation not being linear over many octaves as is necessary.[4]

Modulation instability is where energy is transferred from two fields, ω_1 and ω_2 to two other fields, ω_3 and ω_4. This can be illustrated by examining one term from Eq. 3.30,

$$P_4 \propto \chi^{(3)} E_1 E_2 E_3^* e^{(i\Delta\beta z - \Delta\omega t)}, \tag{3.31}$$

where

$$\Delta\omega = (\omega_1 + \omega_2) - (\omega_3 + \omega_4) \tag{3.32}$$

$$\Delta\beta = (\beta_1 + \beta_2) - (\beta_3 + \beta_4). \tag{3.33}$$

Eq. 3.32 is energy conservation of the process while Eq. 3.33 represents conservation of momentum. Generally, the total momentum of the fields must be conserved, which includes the transverse momentum, but in the paraxial approximation the momentum is along the fiber axis, which simplifies the equation to propagation constants. Eq. 3.33 is called the phase-matching conditions for the fields and is achieved by tailoring the medium and the frequencies used. The propagation constants depend directly on the index of refraction of the medium at the frequencies involved. If the fields ω_1 and ω_2 are independent fields incident upon the medium, the process of creating fields at ω_3 and ω_4 is called phase

[4]Some groups are working toward this goal by employing different modes, where the input modes and output modes do not have the same spatial profile in order to tailor phase matching appropriately [57].

conjugation for historical reasons. If $\omega_1 = \omega_2$ and fields are created at ω_3 and ω_4, the process is called modulation instability.

Bragg scattering occurs when two fields with large intensities are incident at frequencies ω_1 and ω_3 with a weak field inserted at frequency ω_2. In this case, a portion of the fields at frequencies ω_1 and ω_2 are converted to energy in fields ω_3 and ω_4. The efficiency of conversion depends on factors such as the powers of the strong fields, fiber length, phase matching, and bandwidths of the fields. If a quantum state is inserted instead of the weak classical field, it is still possible to translate the energy to a different frequency while preserving the quantum information of the state [58, 37].

3.5. Classical Modulation Instability

In order to describe the process of modulation instability, let us start with an electric field incident upon the optical fiber, polarized in the $\hat{x}$ direction. We will examine the case were the created fields are co-polarized with the pump, although the formalism is very similar for the case where the pump field is orthogonal to the created fields. In a cross polarized configuration, the third order electric susceptibility is decreased by a factor of three, but the final equations are the same. We assume that the pump field has an input transverse spatial profile that is symmetric and has an area of A_{eff}. Then the input electric field is only a function of (z, t)

$$E(z,t) = A(z,t)e^{i(\beta_j z - \omega_j t)} + c.c. \tag{3.34}$$

Here $A(z,t)$ is the amplitude function of the field and satisfies the nonlinear Schrödinger equation [59]

$$-i\partial_z = \beta(i\partial_t)A + \gamma|A|^2A, \tag{3.35}$$

where $\beta(i\partial_t)$ is the Taylor expansion of the dispersion and γ is the nonlinear parameter. Higher-order effects such as group velocity dispersion (GVD) and third order dispersion (TOD) result from expanding $\beta(i\partial_t)$. However, we will be working with pulses longer than 10 ps and will neglect these effects. The nonlinear parameter is defined as

$$\gamma = \frac{n_2\omega}{cA_{\text{eff}}}. \tag{3.36}$$

This comes from solving the nonlinear wave equation, Eq. 3.17. In general, the nonlinear parameter depends on the frequency of the carrier wave, but for this dissertation the frequencies are relatively close together, allowing the parameter to be approximated as a constant, independent of frequency. This last term on the right describes the effect of SPM on the input pump pulse as described above.

For simplicity, we will assume that the fields are quasi-CW, or that the fields are all overlapped in time and are moving together. Then the time components of the field can be ignored and considered to be a global phase shift. For an input field, at frequency ω_1 with incident optical power P_1, the solution to Eq. 3.35 is

$$A(z,t) = \sqrt{P_1}\exp[i(\phi_1(z) - \omega_1 t)], \tag{3.37}$$

where the phases of the fields are

$$\phi(z) = \beta(\omega_1)z + \gamma(P_1)z. \tag{3.38}$$

The effects of SPM on the pump field is apparent in the phase of the pump field in Eq. 3.38. With an equation for the pump, we can derive equations for the sideband fields created by the pump present in an optical fiber. Let the created fields be defined as

$$A_j(z,t) = B_j(z)\exp[i(\phi(z) - i\omega_j t)], \tag{3.39}$$

where $B_j(z)$ is the slowly varying envelope of the sidebands. The signal, idler, and pump frequencies must satisfy the relation derived above

$$2\omega_1 = \omega_s + \omega_i. \tag{3.40}$$

After inserting Eq. 3.39 into the NLS Eq. 3.35 and performing a few steps of algebra, we are left with the coupled wave equations for the signal and idler fields

$$\frac{dB_i}{dz} = i(\beta_i - \beta_p + \gamma P_1)B_i - i\gamma P_1 B_s^* \tag{3.41}$$

$$\frac{dB_s}{dz} = i(\beta_s - \beta_p + \gamma P_1)B_s + i\gamma P_1 B_i^*, \tag{3.42}$$

where $\beta_j = \beta(\omega_j)$ is the propagation constant at the j frequency. Solving these two coupled equations yields the final equations governing the power of the signal and idler fields through the fiber. For simplicity, we assume that the input is only in the

idler field. The solutions with this boundary condition are

$$P_i(z) = 1 + \left(\frac{\gamma P_1}{\kappa_{MI}}^2\right) \sin^2(\kappa_{MI} z) \tag{3.43}$$

$$P_s(z) = \left(\frac{\gamma P_1}{\kappa_{MI}}^2\right) \sin^2(\kappa_{MI} z), \tag{3.44}$$

where κ_{MI} is the phase mismatch between the fields, defined as

$$\kappa_{\mathrm{MI}} = \sqrt{\left(\frac{\Delta\beta_{\mathrm{MI}}}{2}\right)^2 - (\gamma P_1)^2}. \tag{3.45}$$

$\Delta\beta_{\mathrm{MI}}$ is the phase mismatch for modulation instability that includes the material, waveguiding, and nonlinear dispersion

$$\Delta\beta_{\mathrm{MI}} = \beta_s + \beta_i - 2\beta_p + 2\gamma P_1. \tag{3.46}$$

The evolution of the signal and idler fields is sinusoidal with propagation length. This results from the time reversibility of the process: there is no reason for energy to move from the pump to the signal and idler field, but not from the signal and idler to the pump in the undepleted pump regime. Therefore, for optimal energy conversion to the signal and idler fields, one must take care to account for the length of fiber, input pump power, and dispersion properties.

It is important to note that this derivation was performed in the classical limit. Furthermore, the boundary condition of having the idler field present at the entrance of the fiber was used to solve for the evolution of the signal and idler field strengths. To study this effect in the quantum regime, we would like to have a theory that requires no input field in the signal channel. In fact, the case were light is spontaneously produced in the signal and idler channel is the situation

of interest. To move to the quantum regime, it is necessary to begin with the nonlinear polarization and develop the Hamiltonian from that point.

3.6. Spontaneous Four-Wave-Mixing

To examine the spontaneous creation of photons in the signal and idler channel, we begin from the nonlinear polarization. Modifying Eq. 3.22, we find the interaction Hamiltonian for the system is

$$\mathcal{H}_{int} = \chi^{(3)} \int dt \int dV E_p E_q \hat{E}_s \hat{E}_i + h.a. \tag{3.47}$$

Here, the pump fields are E_p and E_q and assumed to be classical and gaussian fields in frequency

$$E_{p,q}(x,y,z,t) = A_0 u_0(x,y) e^{-\frac{(\omega-\omega_{p,q})^2}{2\sigma_{p,q}^2}} e^{i(\beta_{p,q} z - \omega_{p0,q0} t)}, \tag{3.48}$$

where A_0 is the input amplitude of the electric field and $u_0(x,y)$ is the spatial distribution of the field. For complete generality, the two pump fields are labeled differently, although in the case of MI, the fields are in fact the same. The signal and idler fields are quantum fields, labeled by $\hat{E}_{s(i)}$, where the operator nature arises from quantizing the electric field

$$\hat{E}_j(x,y,z,t) = \int d\omega_j e^{i(\beta_j z - \omega_j t)} u_j(x,y) \sqrt{\frac{\hbar\omega_j}{\epsilon_0}} a_j^\dagger(\omega_j). \tag{3.49}$$

Inserting Eq. 3.48 and Eq. 3.49 into the interaction Hamiltonian yields

$$\mathcal{H}_{int} = \chi^{(3)}\mathcal{R}\int d\omega_p \int d\omega_q \int d\omega_s \int d\omega_i \int dz \int dt$$
$$\times \mathcal{E}_p\, \mathcal{E}_q \Phi(\omega_p, \omega_q, \omega_s, \omega_t) e^{-i\Delta\omega t} + h.a., \tag{3.50}$$

where $\mathcal{R}$ is the overlap integral of the spatial profiles for the fields, $\mathcal{E}_{p(q)}$ is the gaussian profile of the pump field, Φ is the phase-matching function, and $\Delta\omega = \omega_p + \omega_q - \omega_s - \omega_i$. Since the integral over time extends to all time, the last factor becomes a delta function

$$\int dt\ \exp[-i(\omega_p + \omega_q - \omega_s - \omega_i)t] \Rightarrow \delta(\omega_p + \omega_q - \omega_s - \omega_i). \tag{3.51}$$

Inserting Eq. 3.51 into Eq. 3.50 causes the integral over $d\omega_q$ to be evaluated at the frequency $\omega_q = \omega_s + \omega_i - \omega_p$. Integrating out ω_q causes the phase-matching function to depend on the frequencies $\Phi(\omega_p, \omega_s + \omega_i - \omega_p, \omega_s, \omega_i)$.

The only term that depends on the propagation distance is the phase term with the combinations of the propagation constants for all the fields. Computing this integral leaves a sinc function times a phase factor dependent on the phase mismatch and the length of the fiber

$$\int_0^L dz e^{\Delta\beta z} = \exp\left[i\frac{\Delta\beta L}{2}\right] \mathrm{sinc}\left(\frac{\Delta\beta L}{2}\right). \tag{3.52}$$

Since the nonlinear interaction is small compared to the linear behavior in the fiber, the wave function can be solved via perturbation theory [60]. The state

becomes [61]

$$|\psi(t)\rangle = |0\rangle_s |0\rangle_i + \epsilon \int d\omega_s \int d\omega_i \, \varphi(\omega_s, \omega_i) \hat{a}_s^\dagger(\omega_s) \hat{a}_i^\dagger(\omega_i) |vac\rangle \,, \tag{3.53}$$

where ϵ is defined to contain the constants including the electric susceptibility, spatial overlap function, and the pump field strengths. The function $\varphi(\omega_p, \omega_s + \omega_i - \omega_p, \omega_s, \omega_i)$ is the joint spectral amplitude, (JSA) [50]. Photon pairs created via SFWM have a spectral distribution that depends on the JSA. The JSA is the product of the pump functions and the phase-matching function

$$\begin{aligned}\varphi(\omega_p, \omega_s + \omega_i - \omega_p, \omega_s, \omega_i) = \int d\omega_p \, \exp\left[-\frac{(\omega_p - \omega_{p0})^2}{2\sigma_p^2}\right] \exp\left[-\frac{(\omega_s + \omega_i - \omega_p - \omega_{p0})^2}{2\sigma_p^2}\right] \\ \times \exp\left[i\frac{\Delta\beta L}{2}\right] \mathrm{sinc}\left(\frac{\Delta\beta L}{2}\right).\end{aligned} \tag{3.54}$$

In frequency space, the pump is a gaussian function that is anti-diagonal, as shown in Fig. 3.4(a). For a given pump frequency, an increase (decrease) in the signal frequency causes a decrease (increase) in the idler frequency to maintain energy conservation, shown above in Eq. 3.40. The width of the pump function inversely depends on the bandwidth of the pump. Tuning the bandwidth of the pump is one method for tuning the factorability of the created photon pair, as we further develop below.

The phase-matching term in the JSA depends on both the dispersion of the fiber (which determines the propagation constants of the light) and the fiber length. An example for a 0.5m segment of Fibercore HB750 is present in Fig. 3.4(b). In general, the phase mismatch, $\Delta\beta$ can be quite complicated, depending on the waveguide and material dispersion of the fiber. For pulses of light that are shorter

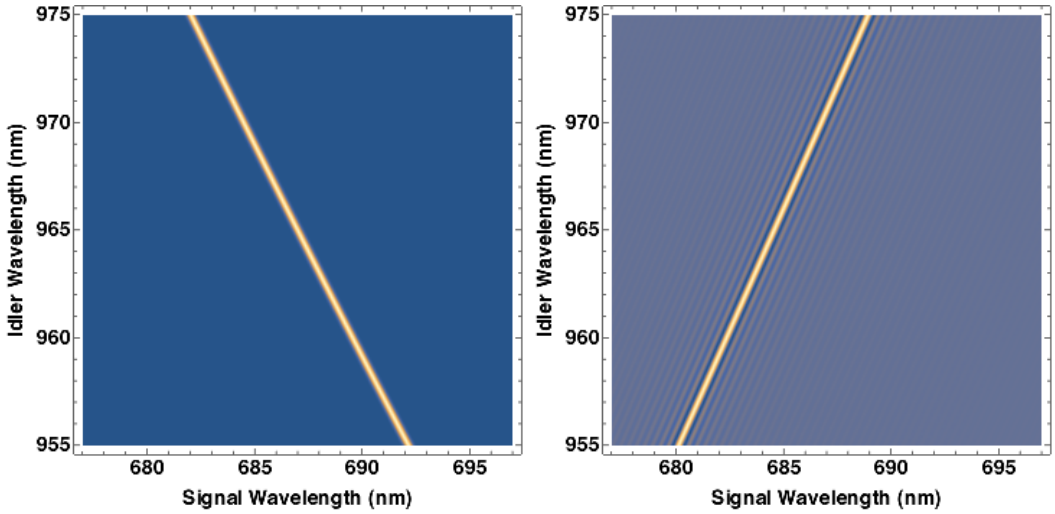

(a) (b)

FIGURE 3.4. (a) Spectrum for a pump with a pulse duration of 3.5 ps. The width is directly determined by the pulse duration. (b) Phase matching function for Fibercore HB750 fiber of length 0.5m.

than $\sim 1ps$, it is important to take higher order dispersion, such as GVD and TOD, into account. However, since this work is focused on pulses that are longer than $30ps$, we can approximate the phase-matching term to be the same as described above in Eq. 3.46.

The width of the phase-matching function inversely depends on the fiber length. However, unlike the pump function, the phase-matching function is not forced to be at a forty-five degree angle in frequency space. The angle relative to the horizontal axis, θ_{si}, results from the dispersion. Specifically, the angle depends on the first derivative of the propagation constant of the pump, signal, and idler fields [50]

$$\theta_{si} = -\arctan\left(\frac{\beta^1(\omega_p) - \beta^1(\omega_s)}{\beta^1(\omega_p) - \beta^1(\omega_i)}\right). \tag{3.55}$$

Here $\beta^1(\omega_j) = \partial\beta/\partial\omega|_{\omega_j}$ is the *group slowness*.

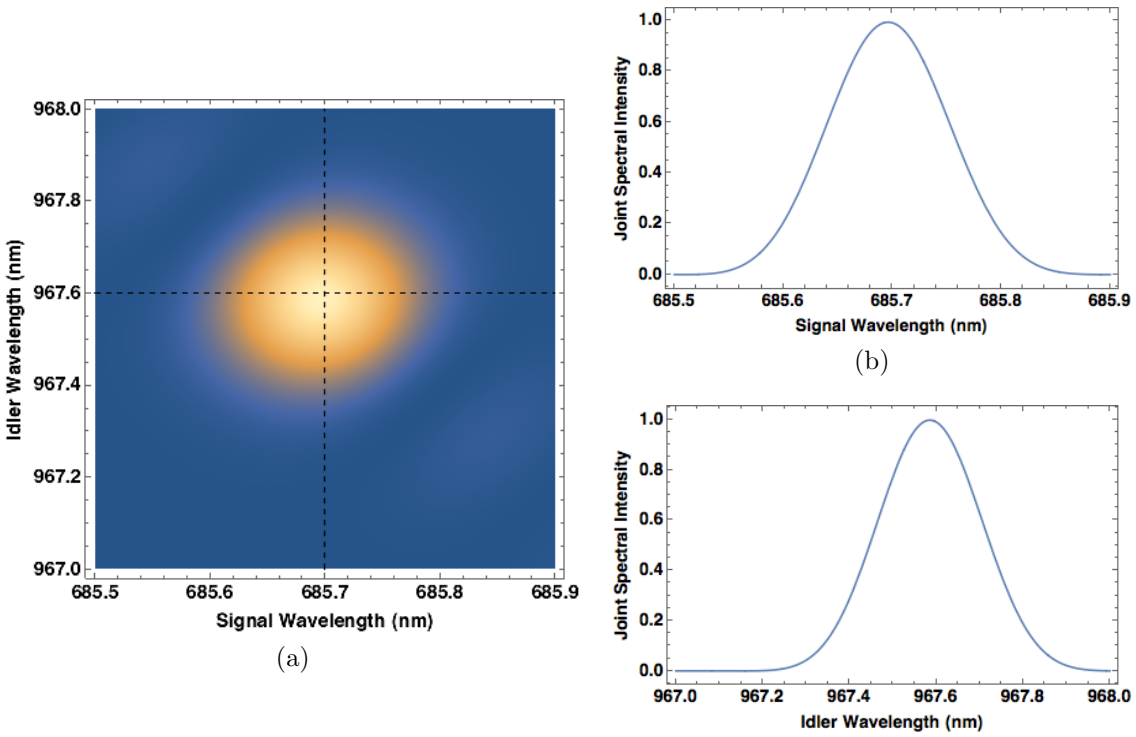

FIGURE 3.5. (a) Joint spectral intensity for a 0.5m segment of HB750 fiber pumped by a laser with pulse duration of 3.5ps, as shown in Fig. 3.4. The dashed lines correspond to the slices plotted in (b) and (c). (b) Slice of the JSI at the Idler wavelength of $\lambda_i = 967.6$ nm. (c) Slice of the JSI at the signal wavelength $\lambda_s = 685.7$ nm.

In order to produce factorable states, it is important to carefully choose a fiber length that matches the pump bandwidth with a dispersion profile that has the phase mismatch at zero with frequencies that conserve energy. Then the joint spectral intensity (JSI) will appear to be a product of a function only dependent upon the signal frequency times a function only dependent upon the idler frequency. The JSI is the modulus square of the JSA. An example of the JSI for a factorable state is plotted in Fig. 3.5(a). Line plots of the JSI along slices through signal and idler frequencies are shown in Fig. 3.5(b) and Fig. 3.5(c).

If the group slowness of the pump and signal are matched, the angle of the phase-matching function will be 0, causing a horizontal line. Conversely, if the idler and and pump have the same group slowness, then the angle will be $-90°$. In this work, we are interested in the case where the phase-matching function is at $45°$ relative to the horizontal. This is achieved when the argument of $\arctan(x)$ is -1. Thus, the difference in group slowness is the same in magnitude between the pump and the signal and idler, but the sign is opposite

$$\beta^1(\omega_p) - \beta^1(\omega_s) = -\left(\beta^1(\omega_p) - \beta^1(\omega_i)\right). \tag{3.56}$$

By convention, the signal field has a higher energy than the idler field, $\omega_s > \omega_p > \omega_i$. In materials with normal dispersion, the index of refraction monotonically follows frequency. Therefore, $n(\omega_s) > n(\omega_p) > n(\omega_i)$. In fact, it is impossible for nonlinear interactions to occur where all frequencies are in the normal dispersion region without a method of modifying the dispersion [62]. In crystals, for example, the optic axis is rotated with a given frequency to impart a crystal defined momentum to offset the phase-matching and overcoming the difference between the propagation constants of the fields. In photonic crystals, it is possible to utilize frequencies that are in both the anomalous region and the normal region in order to achieve phase-matching and energy conservation.

Alternatively, the use of birefringence can be used with a normal dispersion material in order to change the dispersion of certain fields involved in the nonlinear interaction. In this work, birefringent optical fibers will be used to create photon pairs. As described previously, a birefringent optical fiber has two effective indices of refraction, one for each linear polarization in the transverse spatial profile. Birefringent optical fibers are common in telecommunications, marketed

as polarization-maintaining, for having low crosstalk between the transverse linear polarizations along the fiber length. As a result, these fibers are cheap and readably available, making them a useful source for nonlinear photon creation. Furthermore, the dispersion properties fit the desired restrictions stated above, creating symmetric phase-matching over a broad range of pump frequencies accessible by our titanium sapphire lasers.

In a birefringent configuration, there are two main effects on the phase-matching function, $\Delta\beta$: the fields along the slow axis of the fiber experience a linear shift in the index of refraction; and the strength of the self- and cross-phase modulation from the pump is reduced by a factor of 3 [63]

$$\Delta\beta_{BMI} = \frac{2n(\omega_p)\omega_p}{c} - \frac{n(\omega_s)\omega_s}{c} - \frac{n(\omega_i)\omega_i}{c} + 2\frac{\Delta n\omega_p}{c} + \frac{2}{3}\gamma P, \tag{3.57}$$

where Δn is the birefringence.

In this work, the pump is oriented along the slow axis and the signal and idler photons are along the fast axis. This configuration allows for the pump, signal, and idler fields to exist in the normal dispersion region of the fiber. Additionally, the frequency shift between the pump and created fields can be quite large, on the order of 50 THz, which pushes the created fields away from the main Raman peak, which is 13.2 THz below the pump frequency and decreases the contamination from unwanted Raman photons [64, 65]. Orthogonal fields also allows for the practical consideration of filtering the pump field from the produced fields after the fiber, which can be challenging since all the fields are co-propagating out of the fiber.

In the regime of symmetric phase-matching, with the width of the phase-matching and pump functions well matched, then it is possible to produce factorable states, also called separable states. Factorable states result when it

is possible to construct the JSA as the product of two functions, each that only depends on the signal or idler frequency. As a result, the state would change from Eq. 3.53 to a less complicated function,

$$|\psi(t)\rangle = |0\rangle_s |0\rangle_i + \epsilon \left(\int d\omega_s F_s(\omega_s) \hat{a}_s^\dagger(\omega_s) \right) \left(\int d\omega_i \, F_i(\omega_i) \hat{a}_i^\dagger(\omega_i) \right) |vac\rangle \,, \qquad (3.58)$$

where $F_j(\omega_j)$ are functions defining the spectral properties of the signal and idler fields. If the state is factorable, then a measurement of one photon from a created pair does not affect the other photon in the pair. This is important for quantum information processing [23], where it is necessary to measure one photon from the pair of created photons without affecting the other. Additionally, factorable states have a high purity, or only have one Schmidt mode [66], which is a temporal mode of the photons created.

In the gaussian approximation to the phase matching function of the fiber, it is possible to create a perfectly factorable state. However, since the phase matching function is a sinc function, there are tails that do not go to zero. As a result, the real purity is decreased slightly. It is possible to decrease the effect of the tails with filters in frequency with hard edges before the first lobes in order to increase the purity, at the cost of count rates [28]. This has been shown in birefringent fibers that used polarization controllers to adjust the spectrum of the created photons and then filtering to increase the purity of the states created in two different fiber segments [67].

We are interested in created photons in only one Schmidt mode to increase the separability of the photon pairs created and most importantly, create photons that match the modes of the Bragg Scattering process to maximize conversion efficiency.

3.7. Bragg Scattering

By contrast to degenerate modulation instability described above, Bragg scattering (BS) is a four-wave mixing process that utilizes two pumps of different frequency. The BS process is depicted in Fig. 3.6. In BS, one photon from the signal field and one pump photon are annihilated in the fiber and the created photons are in the other pump and idler channel, $s + P_1 \rightarrow t + P_2$.

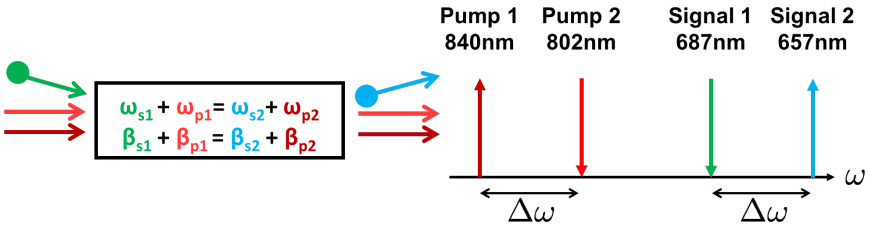

FIGURE 3.6. Diagram of energies involved in Bragg scattering. The downward arrow indicates a photon being annihilated from that field and the upward arrow indicates photons being created into that field. In this schematic, a photon from pump 2 and signal 1 are annihilated, creating a photon in pump 1 and signal 2. The photon in signal 2 preserves the encoded information of signal 1 through the process.

Bragg scattering is similar to processes in $\chi^{(2)}$ materials such as sum frequency generation (SFG) and difference frequency generation (DFG). However, in the case of third-order materials, one has an extra parameter to tune in choosing the frequencies of the fields involved in the nonlinear interaction. By tuning the frequencies of the pump fields, one can change the frequency of the translated field. Care is still required regarding the dispersion of the third-order medium to ensure phase matching between the four fields. This is in contrast to nonlinear interactions in second-order media, where there is only one pump and thus this extra tunability of the translated frequency is lost.

The classical equations for the signal and translated fields are similar to the fields in modulation instability, but the fields are conjugates. This results from

the creation of one field while one field is annihilated. The equations in the fiber are [59]

$$d_z A_s = i(\beta_s - \beta_p + \gamma P_1)A_s + 2i\gamma\sqrt{P_1 P_2}A_t \tag{3.59}$$

$$d_z A_t = i(\beta_t - \beta_p + \gamma P_2)A_t + 2i\gamma\sqrt{P_1 P_2}A_s. \tag{3.60}$$

The solutions to these equations are similar to the solutions for MI in Eq. 3.43 and Eq. 3.44, but with a key difference. In MI, both fields increased together, but in BS, one field increases at the cost of the other. With initial conditions of vacuum in the translated field and unity in the signal field, $A_s(0) = 1$ and $A_t(0) = 0$, the solutions for the fields yield the optical fibers as a function of length

$$P_s(z) = 1 - \left(\frac{4\gamma^2 P_1 P_2}{\kappa_{BS}^2}\right)\sin^2(\kappa_{BS} z) \tag{3.61}$$

$$P_t(z) = \left(\frac{4\gamma^2 P_1 P_2}{\kappa_{BS}^2}\right)\sin^2(\kappa_{BS} z), \tag{3.62}$$

where κ_{BS} is the phase mismatch for BS, defined as

$$\kappa_{BS} = \sqrt{\left[(\beta_t - \beta_s)/2 + \gamma(P_2 - P_1)/2\right]^2 + 4\gamma^2 P_1 P_2}. \tag{3.63}$$

It is clear that the sum of these powers add to 1, or written another way $P_s(z) = 1 - P_t(z)$. The optical power oscillates between the two fields through the length of the fiber and yields the optimal length for translation at $z_{max} = (2j+1)\pi/2\kappa_{BS}$, were j is an integer. If the fiber is equal to z_{max}, the power will be completely transferred to the translated field.

In the quantum case, the pump fields are assumed to be classical fields and remain unchanged in the interaction. In reality, there will be a few photons being

added to one pump and subtracted from the other, but the undepleted assumption is valid since the pumps are strong at the entrance of the fiber. The Hamiltonian of the system is given by [68]

$$\mathcal{H} = \kappa \left(a_s^\dagger a_s - a_t^\dagger a_t \right) + \eta a_s^\dagger a_t + \eta^* a_s a_t^\dagger, \tag{3.64}$$

where κ is the wavevector mismatch and η quantifies the coupling induced by the pump. a_j are operators of the electric fields for the signal and translated fields. The Heisenberg equations of motion are used to determine the behavior of the operators along the length of the fiber, $d_z a_j = i\left[a_j, \mathcal{H}\right]$. The operators exhibit the commutation relations of $[a_j, a_k] = 0$ and $\left[a_j, a_k^\dagger\right] = \delta_{jk}$, where δ_{jk} is a Kronecker delta. Using Eq. 3.64 and the Heisenberg equations of motion yield the solutions of the operators

$$a_s(z) = \tau(z) a_s(0) + \rho(z) a_t(0) \tag{3.65}$$

$$a_t(z) = -\rho^*(z)_s(0) + \tau^*(z) a_t(0), \tag{3.66}$$

where the coefficients are

$$\tau(z) = \cos\left[\left(|\kappa|^2 + \eta^2\right)^{1/2} z\right] + i \frac{\kappa}{\left(|\kappa|^2 + \eta^2\right)^{1/2}} \sin\left[\left(|\kappa|^2 + \eta^2\right)^{1/2} z\right] \tag{3.67}$$

$$\rho(z) = i \frac{\eta}{\left(|\kappa|^2 + \eta^2\right)^{1/2}} \sin\left[\left(|\kappa|^2 + \eta^2\right)^{1/2} z\right]. \tag{3.68}$$

The coefficients are the transfer functions for the solutions of the operator equations of motion. Furthermore, these transfer functions are very similar to the coefficients in the case of light incident on a beamsplitter. Energy is conserved in

the process by requiring that $|\tau|^2 + |\rho|^2 = 1$, which also causes the BS interaction to be unitary.

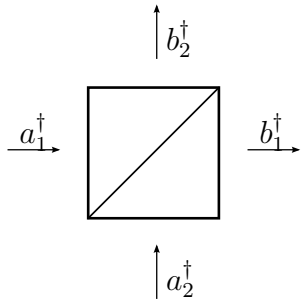

FIGURE 3.7. Diagram of a standard beamsplitter. (a_1, a_2) are the input channels while (b_1, b_2) are the output channels.

For comparison, the input-output relations for a typical beamsplitter, with inputs (a_1, a_2) and outputs (b_1, b_2) as shown in Fig. 3.7, are

$$a_1^\dagger = tb_1^\dagger + rb_2^\dagger \tag{3.69}$$

$$a_2^\dagger = -rb_1^\dagger + tb_2^\dagger. \tag{3.70}$$

The coefficients for the transfer equations in the BS case are the same as the coefficients for the standard beamsplitter. A simple analogy between the BS interaction and a beamsplitter is light interacting with a moving beamsplitter. If the light transmits through the moving beamsplitter, the frequency is unchanged. However, the light reflected is reflected with a doppler shift from the beamsplitter moving [69]. BS has been shown to preserve the quantum properties of the input state while changing the frequency.

As an example, we will show the outcome for a single photon state input into the fiber. The input state can be written as $|\psi\rangle_{in} = a_{s,in}^\dagger |vac\rangle = |10\rangle$ where the state is defined as $|n_s n_t\rangle$ with n_s is the number of photons in the signal field and n_t

is the number of photons in the translated field. Using the transfer functions in Eq. 3.65 provides the output state after the BS interaction in fiber of length L

$$\begin{aligned} |\psi(L)\rangle_{out} = a^{\dagger}_{s,in}\,|vac\rangle_{out} &= \left[\tau(L)a^{\dagger}_{s}(0) + \rho(L)a^{\dagger}_{t}(0)\right]|vac\rangle_{out} \\ &= \tau(L)\,|10\rangle_{out} - \rho^{*}(L)\,|01\rangle_{out}\,. \end{aligned} \tag{3.71}$$

If the phase mismatch, the pump properties, and fiber length are chosen judiciously, it is possible to create an output state that is perfectly translated, where $|\tau(L)| = 0$ and $|\rho(L)| = 0$. Although, the translated state receives a phase of $\phi = l\,[\pi - \arg(\rho)]$, where l is the number of photons in the input state, the translated state is still a perfectly translated copy of the input signal photon state. In this case, an absolute phase is without physical meaning and therefore the phase is arbitrary. The imparted phase depends on the pump fields. It is important to note that in order to create a state that is a pure superposition of the input and translated frequencies, the pump fields must have stationary phases. If the phases are not constant, then the created state becomes a mixed state, with a phase averaged over all the possible phases imparted by the pumps. This example is illuminating and presents the framework for comparing the process of BS to a single-photon input for a typical beamsplitter. However, this assumed that the fields involved were CW. The experiments performed in this work will be with pulses of light, not CW. Therefore, we need to extend this analysis to the case of pulsed pumps and signals.

In general, the operators expanded in frequency are [70]

$$a^{\dagger}(\omega) \rightarrow \int d\omega' G(\omega,\omega')a^{\dagger}(\omega'). \tag{3.72}$$

The Green's kernel in Eq. 3.72 follows the standard orthogonality relations of the form

$$\int d\omega' G(\omega, \omega') G^*(\omega'', \omega') = \delta(\omega - \omega''). \tag{3.73}$$

To complete the relation between the general BS case and a typical beamsplitter, we need a correspondence between the original beamsplitter relations and the Green's kernels for the signal and translated fields. For an input signal field, there are two outcomes during the BS process: translation in frequency or remaining unchanged (reflection or transmission for a standard beamsplitter). Therefore, we can write the operator for the signal and translated field at the end of the fiber as a sum of the processes that result in that field. Explicitly, for the signal field, it will be the sum of photons that were translated from the other field and photons that were unchanged through the process [69, 71],

$$a_s^\dagger(\omega_s) \to \int d\omega_s' G_{ss}(\omega_s, \omega_s') a_s^\dagger(\omega_s') + \int d\omega_t G_{st}(\omega_s, \omega_t') a_t^\dagger(\omega_t) \tag{3.74}$$

$$a_t^\dagger(\omega_t) \to \int d\omega_t G_{ts}(\omega_t, \omega_t') a_t^\dagger(\omega_t') + \int d\omega_t' G_{tt}(\omega_t, \omega_t') a_t^\dagger(\omega_t'), \tag{3.75}$$

where the subscripts of the Green's kernels denote the beginning frequency (right index) and the final frequency (left index). The Green's kernels in Eq. 3.74 and Eq. 3.75 can be arranged into a transfer matrix to take input fields in ω_s and ω_t to output fields in those frequencies

$$\begin{bmatrix} G_{ss}(\omega_s, \omega_s') & G_{st}(\omega_s, \omega_t') \\ G_{ts}(\omega_t, \omega_s') & G_{tt}(\omega_t, \omega_t') \end{bmatrix}. \tag{3.76}$$

Again, the kernels G_{jk} define the process of $\omega_k \to \omega_j$. The kernels can be rewritten via a Schmidt decomposition [71]. A Schmidt decomposition is a form of singular value decomposition, which is a generalization of an eigendecomposition for matrices that are not square. The Schmidt decomposition of the kernels are

$$G_{ss}(\omega_s, \omega_s') = \sum_n \tau_n V_n(\omega_s) v_n^*(\omega_s') \tag{3.77}$$

$$G_{st}(\omega_s, \omega_t) = -\sum_n \rho_n V_n(\omega_s) w_n^*(\omega_t') \tag{3.78}$$

$$G_{ts}(\omega_t, \omega_s) = \sum_n \rho_n W_n(\omega_t) v_n^*(\omega_s') \tag{3.79}$$

$$G_{tt}(\omega_t, \omega_t') = \sum_n \tau_n W_n(\omega_t) w_n^*(\omega_t'), \tag{3.80}$$

where the sum is over the mode functions defined as $\{V_n\}, \{W_n\}, \{v_n\}, \{w_n\}$, which are orthonormal sets. We further restrict the values of the coefficients $\rho_n^2 + \tau_n^2 = 1$. The coefficients ρ_n and τ_n are analogous to the beamsplitter coefficients of reflection (translation) and transmission (no translation in frequency). By using Eqs. 3.77-3.80, the input and output operators for the BS process can be rewritten using the expansions from the Schmidt mode decomposition

$$a_s^\dagger(\omega)|_{in} = \sum_n a_n^\dagger V_n(\omega) \tag{3.81}$$

$$a_t^\dagger(\omega)|_{in} = \sum_n b_n^\dagger W_n(\omega) \tag{3.82}$$

$$a_s^\dagger(\omega)|_{out} = \sum_n c_n^\dagger v_n(\omega) \tag{3.83}$$

$$a_t^\dagger(\omega)|_{out} = \sum_n d_n^\dagger w_n(\omega). \tag{3.84}$$

With these modes, the analogy between the input-output operators of the BS process and the standard beamsplitter relations is made

$$a_n^\dagger = \tau_n c_n^\dagger - \rho_n d_n^\dagger \tag{3.85}$$

$$b_n^\dagger = \rho_n c_n^\dagger + \tau_n d_n^\dagger. \tag{3.86}$$

Clearly, the process of Bragg scattering in an optical fiber is analogous to the interaction of a state on a beamsplitter. However, with Bragg scattering, the coefficients are determined by the properties of the fiber and the pump fields. This analogy is a powerful extension of typical input-output theory for beamsplitters that simplifies nonlinear interactions of photon states in optical fibers. As we will describe in Chapter V, this allows us to greatly simplify the interaction to explore Bragg scattering with photon number states with more than one photon.

CHAPTER IV

DOUBLE-HERALDED MEASUREMENTS OF TWO-PHOTON STATES

Photon-number states can be used for creating photonic operations for quantum information sciences. Additionally, the teleportation of quantum states is improved by using conditional number-state detection [72]. Conditionally prepared, or heralded, number states are states where pairs of photons are created and the detection of one half of each pair heralds the presence of the other photon. The nonlinear-optical nature of crystalline waveguide structures [73], silicon waveguides [74, 75], or silica fibers [76, 77] are common methods of creating heralded single-photon states and more recently n-photon states [78, 79]. $\chi^{(3)}$ media are advantageous over $\chi^{(2)}$ waveguide structures for creating sources easily integrable into fiber networks for quantum communication [80, 81], but they tend to suffer from higher levels of unwanted noise photons created by processes such as Raman scattering. Thus, it is important to devise ways to characterize and counteract this noise.

Heralding photons has been shown to effectively increase the probability of measuring the other photon of the pair [10, 82, 33, 35]. Furthermore, heralding is an effective way to mitigate the degradation of the signal beam by uncorrelated noise photons. This can be shown easily by looking at an example. Let the probability of creating a photon pair be ϵ and let us assume that the probability of creating a noise photon is of the same order. For simplicity, let the probability of creating a noise photon also be ϵ, where $\epsilon \ll 1$. The two photons in the pair are denoted as the herald photon and the signal photon, created via SFWM for example.

Without heralding, the probability of detecting a noise photon or a signal photon from the pair is of the same order. In this case, the measurement of the signal photon will be deeply affected by the presence of the uncorrelated noise photon. The ratio of probability to create a photon pair (P_s) to a noise photon (P_n) goes to $P_S/P_n = \epsilon/\epsilon = 1$.

If we change the measurement to be a heralded detection of the signal dependent upon a detection of the herald photon, the effect of noise is drastically reduced. After heralding, the probability of detecting a signal photon approaches 1 in the ideal case, where there is no loss in the system and the detection efficiencies are unity. Since the process of creating a noise photon is uncorrelated with the photon pair creation, the probability of creating a noise photon remains ϵ. Then the probability of a signal detection resulting from a noise herald is ϵ, which is much less than 1. Additionally, noise in the herald channel for single-heralded photons will cause there to be no photon in the signal channel which will appear to be a decrease in count rates for an experiment, not a fundamental change to the photon number distribution. Therefore, single-heralding is effective at decreasing the effects of uncorrelated noise photons.

Moving to double-heralded generation, the deleterious effects of noise return. The probability of producing two pairs of photons simultaneously is the square of the probability producing a single pair, $P_{2s} = \epsilon^2$. The process of producing two pairs of photons is equal to the probability of producing one pair and one noise photon simultaneously or the probability of producing two noise photons. In this case, the ratio of probabilities of creating 2 photon pairs to the probability of creating a pair and a noise photon is of order 1, $P_{2s}/P_{1s1n} = \epsilon^2/\epsilon^2 = 1$. The effects of noise are again similar to the case of the unheralded photon experiment.

The problem of double-heralding fundamentally arises from the uncorrelated nature of producing two photon pairs. The production of each pair is uncorrelated with the production of the other pair, causing the probability of the production of two pairs to be ϵ^2 in the example above. If the two pairs were correlated in production, it would be possible to utilize this behavior to reduce the noise in double-heralding experiments. Noise for heralding events skews the photon number distribution toward lower photon numbers by increasing the number of herald photons while leaving the signal channel unchanged, making the signal channel appear to be a distribution with a larger photon number than is actually present.

Although double-heralding is susceptible to noise more than single-heralding, double-heralding is still useful for preparing two-photon states. In this chapter, we will show that the effect of noise in the herald channel is equivalent to a loss in the signal channel. Additionally, we will explore a method for measuring the noise and inferring the noise-free photon number distribution.

The method of detecting quantum states described here is independent of the number of modes present in the state being measured. There is no mode-specific sorting occurring in the measurement and in the assumption that all modes are measured with the same efficiency, then the multimode nature of the light has no effect upon the measurement. This is in contrast to mode specific techniques such as quantum state tomography [83, 84, 85, 86], that require Fock states, or single mode states for proper measurement. While this technique does not give full state reconstruction, it does provide important information regarding the photon number distribution without the need for precisely matched local oscillator fields to investigate the state under measurement.

The work presented in this chapter was carried out in collaboration with Dileep Reddy and Dashiell Vitullo [87].

4.1. Spatially-Multiplexed Photon Detection

There are many types of detectors that have recently been developed for the detection of single photons. Superconducting bolometers, cryogenic superconducting wire arrays, and transition edge detectors have all been developed to provide number resolution. However, these types of detectors must be operated at cryogenic temperatures, between 1mK to 10K and have potentially large insertion losses. Alternatively, avalanche photodiodes (APDs) operate at room temperature, have high efficiencies [88], and are relatively inexpensive. APDs are typically utilized in Geiger mode and are thresholding, or do not discriminate between the number of photons incident. The response from an APD is the same for one or more photons. Although APDs are thresholding detectors, it is possible to measure the photon number distribution by direct inversion and sampling the input beam [89, 90, 91, 92, 93, 94, 95, 96]. The sampling can be done either in time or space.

Temporal multiplexing relies on having having multiple optical paths that are combined upon one or two detectors. Each path is equally possible and has a different travel time. The different paths correspond to different time bins that arrive at the detector. In this scheme, it is important to carefully design the experimental apparatus such that the difference in propagation time for each path is longer than the dead time of the detectors. The thresholding detectors used in quantum optics experiments are typically detectors with very high voltage gain, such as an avalanche photodiodes (APDs), and have a dead time after detecting a

photon. If a second photon arrives before the detector has had sufficient time to reset, the photon will not be detected. The dead time is commonly of the order 50 ns. Therefore, it is important that each path is longer than the dead time of the detectors used in the experiment. Furthermore, it is important that pulses of light do not arrive at the temporally multiplexed detectors before all the time bins have been recorded by the detectors. This restriction causes the decrease in possible detection speed in exchange for more time bins.

Spatially multiplexed detection utilizes beamsplitters to divide the input light into many paths that are physically distinct with a detector at the end of each path. This scheme does not suffer from the issue of long wait times between pulses. The time between pulses needs to be slightly longer than the dead time of one detector only, not the product of the number of paths times the detector dead time. In this case, the cost of more detection bins is physical space and a need for more experimental equipment. Spatially multiplexed APDs can be used with high-repetition-rate sources, easily achieving counting rates on the order of MHz. Fig. 4.1 depicts an example of spatially multiplexed detectors.

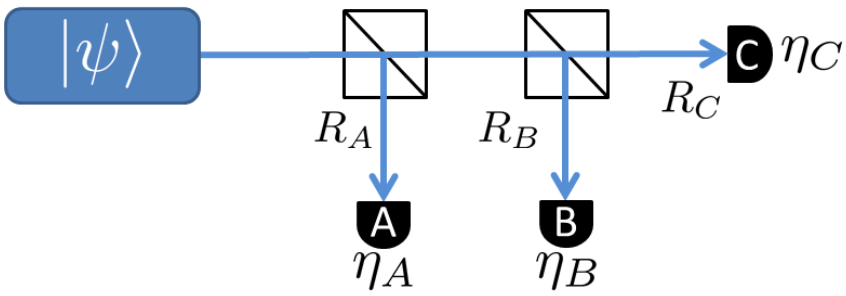

FIGURE 4.1. Spatially multiplexed detector setup with three detectors to approximate a number-resolving detector. Each detector receives a fraction R_i of the light from the original state and has an efficiency of η_i of detecting an incident photon.

The measurements of spatially multiplexed detectors with thresholding detectors are strongly dependent upon the efficiency of detection for each detector and the fraction of the input beam that is directed toward each detector. The non-unity efficiency must be taken into account when inverting the measurement data to determine the input photon number probabilities. The efficiencies of the detectors and the amount of the input state sampled by each detector is used with standard probabilities to define the conditional probability matrix of the detection system. The conditional probability matrix maps detection events into the photon number distribution.

With thresholding detectors, the presence of one or more photons causes the detector to "click" or "fire." The elements of the conditional probability matrix map p_n photon number distribution into q_k clicks. In general, the matrix is of the form [97]

$$\mathbf{q} = \mathbf{C} \cdot \mathbf{p}, \tag{4.1}$$

where $\mathbf{p}$ is the photon number distribution of the input state, $\mathbf{C}$ is the conditional probability matrix, and $\mathbf{q}$ is the matrix of measured clicks from the detectors. For example, if the spatially multiplexed detection system is composed of three detectors, the Eq. 4.1 becomes

$$\begin{pmatrix} q_1 \\ q_2 \\ q_3 \end{pmatrix} = \begin{pmatrix} P(1|1) & P(1|2) & P(1|3) \\ 0 & P(2|2) & P(2|3) \\ 0 & 0 & P(3|3) \end{pmatrix} \begin{pmatrix} p_1 \\ p_2 \\ p_3 \end{pmatrix}, \tag{4.2}$$

where q_k is the probability of k clicks, p_n is the probability of n photons incident upon the system of spatially multiplexed detectors, and the matrix elements $P(k|n)$ are the probability to produce k clicks, given n incident photons. It is assumed that the probability to create photon numbers larger than $n = 3$ is negligibly small. It is important to include enough detectors to measure photon pairs that are larger than the desired photon pair states to be measured. For systems with more than 3 detectors, the matrix is expanded and the vectors $\mathbf{p}$ and $\mathbf{q}$ are extended. This method easily generalizes to larger photon numbers.

The matrix can be extended to include the vacuum term, p_0, but the resulting matrix element would cause the conditional probability matrix to no longer be linearly independent. Instead, the vacuum component is calculated by assuming the probabilities add to unity

$$p_0 = 1 - (p_1 + p_2 + p_3)\,. \tag{4.3}$$

It is not necessary to record which detector or combination of detectors click for a given pulse. It is only important to measure the total number of detections that occur over a given time window containing many pulses. This is incorporated into the elements of the conditional probability matrix. We record many pulses and collect the total counts of single-, double-, and triple-detection events between the three measurement detectors. Through the use of set theory, this data can be combined to determine the equations for one and only one detector firing, two and only two detectors firing, or three and only three detectors firing. This is directly apparent in the matrix elements of the conditional probability matrix. Using this

method, the matrix elements are

$$P(1|n) = \mathscr{P}(A|n) + \mathscr{P}(B|n) + \mathscr{P}(C|n) - 2\left(\mathscr{P}(AB|n) + \mathscr{P}(AC|n) + \mathscr{P}(BC|n)\right) + 3\mathscr{P}(ABC|n) \tag{4.4}$$

$$P(2|n) = \mathscr{P}(AB|n) + \mathscr{P}(AC|n) + \mathscr{P}(BC|n) - 3\mathscr{P}(ABC|n) \tag{4.5}$$

$$P(3|n) = \mathscr{P}(ABC|n), \tag{4.6}$$

where $P(i|n)$ define the probability of i and only i detection events given n incident photons and $\mathscr{P}(l|n)$ is the probability that all detectors in the set l will click, given n incident photons, where $l \in \{A, B, C, AB, ..., ABC\}$. This method drastically simplifies the collection method since there is no need for measuring and recording each individual pulse. Instead, it is possible to measure many pulses while collecting the total number of the different detection events and recover this information.

The non-unity efficiencies and thresholding behavior of the detectors is taken into account directly by the probability that a given set of detectors will click. The probabilities are

$$\mathscr{P}(i|n) = 1 - (1 - R_i\eta_i)^n \tag{4.7}$$

$$\mathscr{P}(ij|n) = 1 - (1 - R_i\eta_i)^n - (1 - R_j\eta_j)^n + (1 - R_i\eta_i - R_j\eta_j)^n \tag{4.8}$$

$$\begin{aligned}\mathscr{P}(ijk|n) =& 1 - (1 - R_i\eta_i)^n - (1 - R_j\eta_j)^n - (1 - R_k\eta_k)^n \\ &+ (1 - R_i\eta_i - R_j\eta_j)^n + (1 - R_i\eta_i - R_k\eta_k)^n + (1 - R_j\eta_j - R_k\eta_k)^n \\ &- (1 - R_i\eta_i - R_j\eta_j - R_k\eta_k)^n,\end{aligned} \tag{4.9}$$

where i, j, k refer to detectors $\{A, B, C\}$, and η_i is the total detection path efficiency for the ith detector and R_i is the fraction of light directed toward that detector, as depicted in Fig. 4.1. η_i includes the transmission losses in the beam path and the quantum efficiency of the corresponding APD. The thresholding nature of the detector creates the terms $1 - (1 - R_i\eta_i)^n$ that determine the probability of detecting a photon. This results from starting with the probability that n photons are not detected at a given detector, i: $(1-R_i\eta_i)^n$. Then subtracting this from one gives the probability that at least one of the n photons is detected at detector i for thresholding detectors [98].

The efficiency in the inversion algorithm is the total efficiency of collection for the detection apparatus. This efficiency includes optical transmission losses through any optical elements (filters, dichroic mirrors, polarizers, etc.), coupling losses in the fibers used to couple the light into the APDs, and the quantum efficiencies of the APDs. Inserting the total efficiency in the inversion algorithm reproduces the true photon number distribution incident upon the spatially multiplexed detectors.

It is of utmost importance that the proper efficiency is used in the inversion algorithm. The output photon number distribution depends sensitively on the efficiency used in the conditional probability matrix. Incorrect estimation of efficiency for the detectors can falsely present a distribution that resembles a one-photon state. In fact, if the efficiency used in the inversion algorithm is higher than the experimental efficiency of the data, the photon distribution will appear to be a one-photon number state when the state under measurement is actually a two-photon number state. Conversely, if the efficiency is underestimated, the photon number distribution will skew toward higher photon numbers. For detectors with lower efficiencies, there must be more photons present in order to register a click

and many clicks will be missed. Lower efficiencies results in clicks having a higher probability of occurring with larger photon numbers. Therefore, experiments with low efficiencies and a large collection of clicks registering that only one and one detector fired will appear to measure photon number states with higher two-photon and three-photon components. An example of the importance of correct efficiency estimation is shown in Fig. 4.2

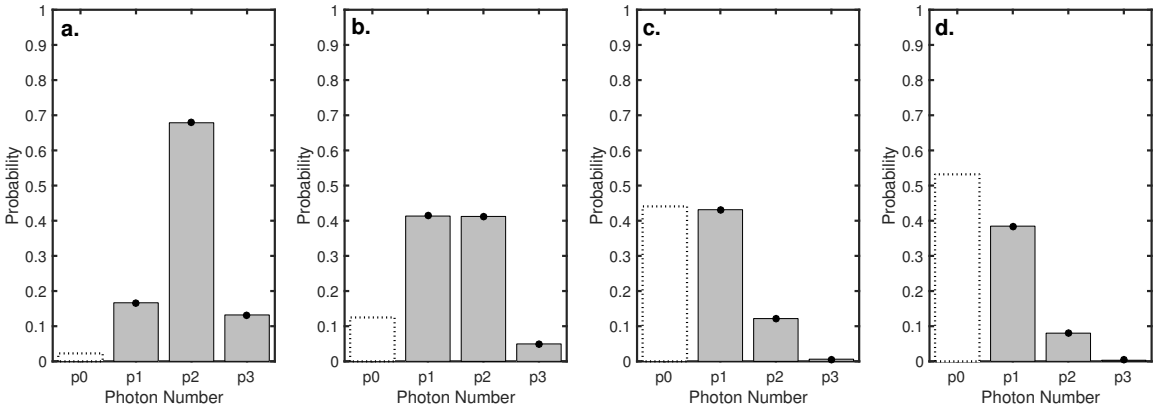

FIGURE 4.2. Photon number probability inversion resulting from the inversion algorithm with different efficiencies in the conditional probability matrix. The source was 10m of HB800 Fiber pumped by 83 mW average power of a 36ps titanium sapphire laser. The efficiencies used in the inversion algorithm were a. Klyshko Efficiency (23%), b. 40%, c. 80%, d. unity efficiency.

Alternatively, noise processes in the source fiber can artificially increase the number of herald channel clicks without affecting the number of signal channel clicks recorded. The resulting measurement appears to be inefficient at measuring signal photons, since there are more herald clicks than signal clicks. As we will discuss in the following section, noise processes in the state preparation decrease the efficiency of detecting photon pairs, allowing the noise to be modeled as decreases in the detection efficiency.

4.2. Effects of Noisy Heralding

For the following derivation, let us begin by describing the source of photons. For example, we will use a source that produces pairs of photons, one labeled as the signal (subscript s) and one labeled the herald (subscript r). The probability of creating photon pairs in the herald and signal channel is denoted by $\bar{P}_{rs}$. We will assume that the herald photon is lower in frequency ($\omega_r < \omega_s$), where the two photons are equally spaced in energy from the pump source. As described in Chapter 3.6, the names are used to label the use of the photons; the herald photon will be used to conditionally prepare signal photons for use in other quantum optics experiments. The use of the bar over the photon probability ($\bar{P}$ instead of P) denotes the noise-free nature of this distribution. We assume there is no noise and $\bar{P}$ only describes the joint probability distribution of signal and herald photons created by a photon pair source. In order to properly conditionally prepare the signal photon, is important to determine the probability of a signal photon, given the detection of a herald photon. Through straightforward probability theory, the conditional probability of a signal photon given a herald photon is

$$\bar{P}_{sr}(n_s|n_r) = \frac{\bar{P}_{rs}(n_s, n_r)}{\sum_{m=0}^{\infty} \bar{P}_{rs}(m, n_r)} = \frac{\bar{P}_{rs}(n_s, n_r)}{\bar{P}_r(n_r)}, \tag{4.10}$$

where $\bar{P}_r$ denotes the noise-free probability distribution in the herald channel.

In order to make this model more realistic, we need to introduce the effects of noise photons. For example, in optical fibers, there is often a large amount of Raman scattering [65] and other nonlinear processes that can begin to change the photon distribution created by the source. Let us assume that noise photons in the herald channel are created by processes independent of the photon pair creation

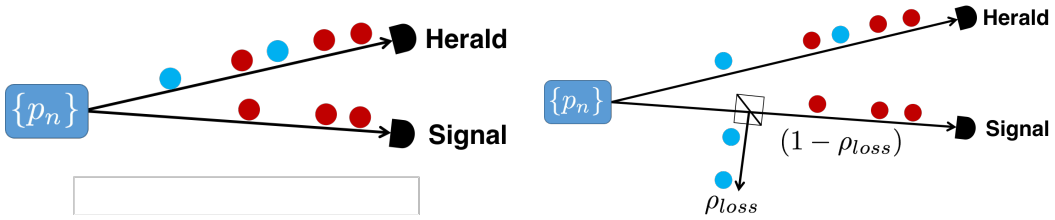

(a) (b)

FIGURE 4.3. (a) Cartoon describing the presence of noise photons (blue circles) in addition to herald photons (red circles) in the herald channel. (b) A schematic of a beamsplitter in the signal channel that acts as a loss. The red photon pairs successfully make it through the beamsplitter, while blue photons are lost. Both physical pictures are described by the same theory, shown in Eq. 4.12 and Eq. 4.13.

process of interest. In this case, the photons in the herald channel are either from the target process or from a noise process. Suppose the probability that the herald photon is from the target process is η_r. A schematic is shown in Fig. 4.3. If k detection events occur, the probability that m detection results from a herald photon becomes a binomial distribution with the probability of herald photon as the success outcome

$$p(m|k) = \binom{k}{m} \eta_r^m (1-\eta_r)^{k-m}. \tag{4.11}$$

With a conditional probability that a herald detection is from noise, we can directly compute the conditional probability that a signal detection results from a given herald detection. Given k_r herald events, the probability of detecting n_s photons is the convolution of Eq. 4.10 and Eq. 4.11 [10]

$$P(n_s|k_r) = \sum_{m=0}^{k_r} \bar{P}_{sr}(n_s|m) p(m|k_r) = \sum_{m=0}^{k_r} \binom{k_r}{m} \eta_r^m \left(1-\eta_r\right)^{k_r-m} \bar{P}_{sr}(n_s|m). \tag{4.12}$$

Alternatively let us examine the situation where there is no noise in the herald channel, but there is loss in the signal channel. In this case, we will use the noise-free conditional probability distribution from Eq. 4.10, $\bar{P}(n_s|n_r)$. However, we will introduce a beam splitter in the signal channel with reflection coefficient ρ_{loss} and thus transmission coefficient $1 - \rho_{loss}$. When photons are incident upon this imposed beamsplitter, the photons must either transmit through the beamsplitter or reflect, considered a loss. Thus, the distribution of photons that make it through the beamsplitter to the signal channel detector is also a binomial distribution convolved with the input photon number distribution

$$P_S(n|k) = \sum_{m=1}^{n} \binom{k}{m} (1 - \rho_{Loss})^m (\rho_{Loss})^{k-m} \bar{P}_{sr}(m|k). \tag{4.13}$$

It is clear from inspection that Eq. 4.12 and Eq. 4.13 are the same if $\eta_r = (1 - \rho_{loss})$, or if the probability that a detection in the herald channel results from the target process is the same as the the probability that a signal photon transmits through a beamsplitter and is detected in the signal channel. This is shown in Fig. 4.3. This directly shows the equivalence between noise in the herald channel and a loss in the signal channel.

Through the equivalence of a signal channel loss and a noisy herald channel, we are able to make straightforward measurements on the photon pairs to estimate the efficiency of heralding and then change the inversion algorithm to account for the contributions from noise. As we will discuss in the following section, this is a powerful tool in understanding the noise present in a photon pair source.

4.3. Efficiency of Measuring Coincidences

As shown in the previous section, proper measurement of the noise in the herald channel can give insight into inferring the noise-free distribution possible from the source under measurement. Furthermore, it is possible to quantify the amount of noise present in the photon pairs created by the source by measuring the efficiency of detecting coincidences from a correlated pair source.

The source investigated here is an optical fiber that produces pairs of photons via SFWM as described in Chapter 3.6. We can exploit the temporal correlation in creation time for the photons to determine the efficiency of measuring coincidences. This efficiency is called the Klyshko heralding efficiency [97], in honor of David Klyshko, who first proposed the method as a means to characterize detectors used for measuring quantum states [99, 100, 101].

For a given pair of detectors measuring the photons from a correlated pair source, the Klyshko heralding efficiency, η_k, is the ratio of the joint probability of measuring both photons divided by the probability of measuring the herald photon

$$\eta_K = \frac{P(H,S)}{P(H)}. \tag{4.14}$$

The Klyshko heralding efficiency is also by definition the conditional probability of detecting a signal photon given a herald photon detection. If the signal and herald channels are free of noise photons, then in a long counting window, the number of coincidence detections and herald detections are, respectively

$$N_{HS} = \eta_H \eta_S \gamma \tag{4.15}$$

$$N_H = \eta_H \gamma, \tag{4.16}$$

where η_H is the detection efficiency of the herald channel (including transmission losses and detector efficiency), η_S is the detection efficiency of the signal channel, and γ is the number of photon pairs produced within the same time interval. By inserting Eq. 4.15 and Eq. 4.16 into Eq. 4.14, we find the noise-free Klyshko heralding efficiency equal to the detection efficiency of the signal channel

$$\eta_K = \frac{P(H,S)}{P(H)} = \frac{N_{HS}}{N_H} = \frac{\eta_S \eta_H \gamma}{\eta_H \gamma} = \eta_S. \tag{4.17}$$

This result is somewhat intuitive; in a perfect experimental system that is without noise, the probability of measuring a signal photon given a herald detection is independent of the herald detection efficiency. However, the addition of noise introduces a factor that decreases the Klyshko heralding efficiency, depending on the amount of noise present in the source.

We assume that the source only produces noise photons in the herald channel. This assumption is reasonable for a cross-polarized phase matching configuration as Raman scattering that is upshifted from the input pump is negligible [65]. Furthermore, this is consistent with experimental observations of the output from our fiber source measured with a highly sensitive liquid nitrogen spectrometer. Due to the noise process being independent of the target process, the noise photons should be uncorrelated with the signal photons and has a negligible effect upon the coincidences.

By examining the source of the noise photons and the photons created through the pair process, we are able to modify the Klyshko heralding efficiency and determine explicitly the contributions of the different noise processes present. The factor that is multiplied by the efficiency of measuring a photon in the signal

channel is

$$\eta_K = \frac{\eta_S \eta_H \gamma}{\eta_H \gamma + \eta_H \sigma} = \eta_S \frac{\gamma}{\gamma + \sigma}, \tag{4.18}$$

where σ is the number of noise photons in the herald channel. We can further expand the denominator by including the noise terms expected from the source.

A pulsed pump with average power P incident upon a finite fiber of length L will produce photon pairs that scales as $N_{MI} \propto P^2 L$. Raman scattering, however, will produce photon pairs linear in power and length, $N_R \propto PL$ [64, 65]. Finally, we introduce a term independent of fiber length that is linear in pump power to account for leakage from the pump field or any other field that is present before the fiber. By combining all these factors, we can construct a new denominator for the Klyshko heralding efficiency

$$\eta_K = \eta_S \times \frac{P^2 L}{P^2 L + \beta P L + \alpha P}, \tag{4.19}$$

where β is the power at which Raman scattering matches the SFWM generation rate, α is defined similarly, and η_S is the total (source independent) system detection efficiency in the signal channel. α has units of power times length.

Luckily, each of the terms in the denominator of Eq. 4.19 have a different dependence upon input pump power and fiber length. By measuring the Klyshko heralding efficiency for a range of input pump powers and fiber lengths, we can fit the parameters for Raman scattering and linear pump noise. With an explicit measure of the contributions from noise processes, one can decide on a method for decreasing the noise present in the photon creation source.

In addition, measuring the Klyshko heralding efficiency is a powerful tool for inferring the noise-free photon number probability distribution created by the source. Since noise in the herald channel is equivalent to a loss in the signal channel, the Klyshko heralding efficiency can be used in the inversion algorithm to account for the effect of noise photons on the photon number probability distribution. As we will see, using η_K in Eqs. 4.7-4.9 produces the inferred, noise-free photon number distribution.

4.4. Experimental Apparatus

A diagram of the experimental setup is shown in Fig. 4.4. The photon source in the experimental setup is a commercially available, PANDA-type birefringent fiber HB800 from Fibercore pumped by a titanium sapphire laser (TiS). The laser is passively modelocked with a semiconductor saturable absorber (SESAM) that produces transform-limited pulses with duration 36 ps. The polarization of the Ti:S is rotated with a half wave plate (HWP) before the HB800 fiber. The polarization of the laser is oriented along the slow axis of the fiber to produce photon pairs in the normal dispersion region of the fiber, as described in Chapter 3.6. With a small probability ($\sim 10^{-6}$), two photons from the incident pump field are annihilated and create a pair of photons. The signal photon is created at an up-shifted frequency from the pump and there herald photon is created at a down-shifted frequency from the pump. The pump field is centered at $\lambda_p = 802$ nm with a bandwidth $\Delta\lambda \approx 10$ pm. The signal photons are centered at $\lambda_s = 687$ nm and herald photons $\lambda_h = 965$ nm, which corresponds to a frequency shift of 437 THz from the pump wavelength. The photon pairs are produced far away from the peak of the Raman gain of 13.2 THz below the pump.

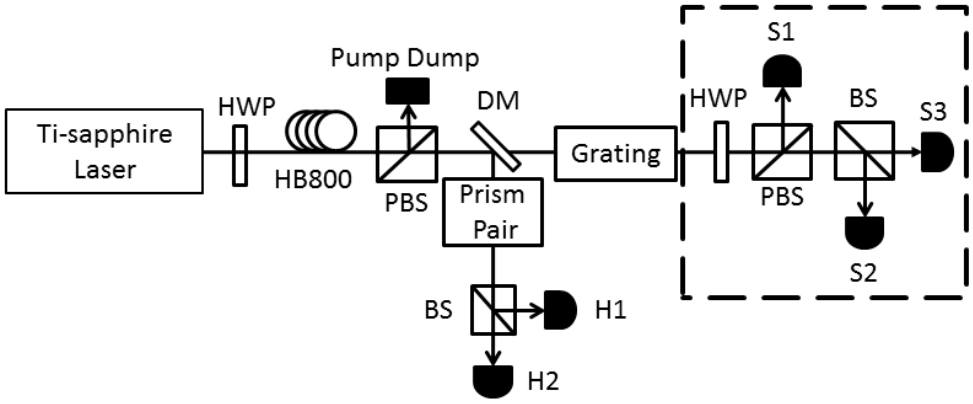

FIGURE 4.4. Experimental setup for measuring conditionally prepared number states. The multiplexed detectors are located within the dashed box. The two heralding detectors and the three signal detectors are connected to an FPGA and a computer for storing data. HWP denotes a half wave plate; DM denotes a dichroic mirror; BS denotes a beamsplitter; PBS denotes a polarizing beamsplitter.

A polarizing beamsplitter is located at the output of the fiber to filter the pump field and pass the photon pairs, which are polarized along the fast axis of the fiber. To measure the Klyshko heralding efficiency, the photon pairs are separated with a dichroic mirror (Semrock FF01-746) that transmits the signal photons and reflects the herald photons. The herald field is further filtered in frequency with a prism pair (SF14 glass) and an iris. The prism pair disperses the herald channel and photons different from the herald photons are blocked by the iris. After the prism pair, the herald beam is split evenly at a 50/50 beamsplitter to two fiber couplers. Multimode GRIN fibers (Thorlabs M31L03) are used to couple the light into APDs.

The signal field is transmitted through the dichroic mirror and is incident upon a blazed grating (2200 lines/mm) for further spectral filtering before the spatially multiplexed detectors. The spatially multiplexed detection system consists of a half wave plate, a polarizing beamsplitter, and a 50/50 beamsplitter. The first HWP is rotated such that the polarizing beamsplitter reflects a third of the

light to a fiber coupler and sends the rest to the 50/50 beamsplitter. The 50/50 beamsplitter equally splits the light to two fiber couplers. All three signal channel fiber couplers are coupled to APDs with multimode GRIN fibers.

Although step-index multimode fibers are much easier to couple into than single mode fibers, the excitation of multiple spatial modes in the fiber can cause a smearing of the pulse by introducing a large time delay between spatial modes. The multimode GRIN fibers were chosen to decrease the time delay between different spatial modes propagating the length of the fiber while providing ease of coupling.

The APDs used to detect the signal and herald photons are used in Geiger mode and from Perkins-Elmer (SPCM-AQ4C). The APDs have a wavelength-dependent quantum efficiency that is approximately 60% for the signal wavelength and 15% for the herald wavelength. Through use of tracer lasers at wavelengths close to the herald wavelength, the efficiency of the herald channel multimode fiber couplers is estimated at 80%.

To measure the transmission efficiency for the signal channel, a similar procedure is used with tracer lasers that are close to the wavelength of the signal photons. However, the dispersive elements in the signal channel cause the measured efficiencies with a tracer beam to be estimates with sizable uncertainty. The total transmission efficiency in the signal channel is estimated to be 36% $\pm$ 5%. This efficiency includes all optical losses from the beamsplitters and filters, multimode fiber coupling losses, and the quantum efficiency for detection at the signal wavelength of the APDs. The efficiency and beamsplitter ratio for the signal detectors are a key component of the inversion algorithm, inserted as the values η_i and R_i, respectively, in Eqs. 4.7-4.9.

When a photon is detected, an APD produces a TTL pulse. The APDs measuring the herald channel are connected to an digital coincidence box that can be set to pass a single APD or coincidences between the herald APDs. The herald coincidence box and the three signal channel APDs are connected to a field programmable gate array (FPGA) that bins the detection events from the APDs. The FPGA records all single detections, coincidences for all possible pairs of detectors, triple, and four-fold coincidences of the signals with the herald channel detectors. This setup allows us to quickly switch between single-heralded measurements and double-heralded measurements. The coincidences are sent to a computer via LabView and the values are stored locally for analysis.

From the theory in Chapter 4.1, we do not need to measure each individual pulse. Instead, we are able to measure a large number of pulses without tracking each pulse. A notable advantage of this approach is the speed of measuring detections. The detection equipment is capable of measuring at rates of a few MHz by binning millions of pulses and storing the total values. The increase is a major advantage for this method over temporal multiplexing.

For a given fiber length, the input pump power was varied between $10 - 50$ mW average power and the single-herald coincidences were measured. By taking the ratio of the coincidences between a single herald and signal detector (e.g. $H1$ and $S1$), with the number of herald detections ($H1$), the Klyshko heralding efficiency is computed for a given pair of detectors. There is a different Klyshko heralding efficiency for all combinations of herald and signal detectors ($H1S1, H1S2, H1S3, H2S1, H2S2, H2S3$). For a given signal detector, the Klyshko heralding efficiency for each herald detector (e.g. $H1S1$ and $H2S1$) was the same within 1%. The three Klyshko heralding efficiencies for the signal channel detectors

were similar in value, within a few percent. This measurement was repeated for four fiber lengths, $L = 5\,\mathrm{m}, 10\,\mathrm{m}, 15\,\mathrm{m}, 20\,\mathrm{m}$.

The Klyshko heralding efficiencies for all fiber lengths and input pump powers were fit to Eq. 4.19. The values and the fits are shown in Fig. 4.5. At a given power and fiber length, there are three points, one for the Klyshko heralding efficiency of each signal detector. At some points, it appears that there are only two or one value, although there are three points. At these locations, the three Klyshko heralding efficiencies are all very close in value. The parameters for the fit in Fig. 4.5 are $\eta_{System} = 41.95\%$, $\beta = 5.324 \times 10^{-6}$ mW, and $\alpha = 344$ mW$\cdot$meters. Eq. 4.19 with these parameters fit all the data, for different fiber lengths and coupled pump power, quite well.

Although the coefficients for the Raman scattering and pump leakage terms are different in units, it is straightforward to make comparisons between the contributions for each process. Since Raman scattering and SFWM depend on length, it is possible to overcome the degradation from pump leakage by using longer fibers for a given pump power. However, for fiber lengths that are shorter than 70×10^6 m, the pump leakage will dominate the Raman contribution at any pump power. A fiber of such a length used as a photon pair source would be extremely impractical as the phase-matching would render it nearly impossible to tailor a pump to create factorable states. Additionally, the fiber losses would become quite significant for lengths of this order.

Comparing the pump leakage term to the SFWM term provides a range in which the SFWM dominates. For a fiber length of $L = 5$ m, the necessary average pump power is 68.8 mW, which decreases to 17.2 mW at $L = 20$ m. These pump

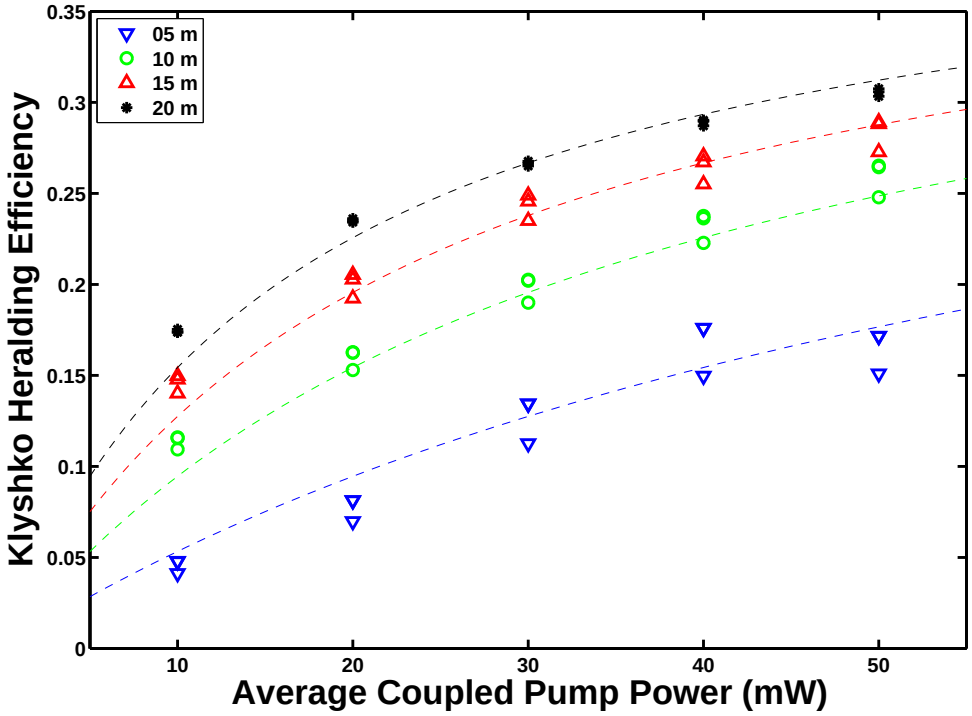

FIGURE 4.5. Measured Klyshko heralding efficiencies for different average pump powers and fiber lengths with the fits to Eq. 4.19 denoted by the dashed lines. There are three points presented for each pump power and fiber length representing the Klyshko heralding efficiency for each signal detector. Some points overlap where values are nearly identical.

powers are quite reasonable and indeed within the experimentally accessible range of pump powers.

As the coupled pump power was increased, the Klyshko heralding efficiencies asymptotically approached the system efficiency. For larger pump powers, the SFWM dominates the noise created by Raman scattering or from pump leakage. For larger lengths, the Klyshko heralding efficiency is closer to the system efficiency for lower pump powers, due to the dependance of the SFWM term on fiber length.

Not only does measuring the Klyshko heralding efficiency give an experimentalist a wealth of information regarding the noise processes present in a photon pair source, this data also allows for the calculation of the noise-free

photon number distribution. That is, one can use the Klyshko heralding efficiency to determine what the photon number distribution created by a given source would be if there were no noise present.

4.5. Measured Photon Number States

The inversion algorithm is applied to the data for zero-, single-, and double-heralded measurements of the signal channels for all the pump powers and lengths used for the Klyshko heralding efficiency measurements of the previous section. A particularly illustrative example of the change in the photon number distributions is for a fiber length of 20m. All of the detection events were multiplied by the inverse of the conditional probability matrix to recover the photon number distribution incident upon the spatially multiplexed detector, as described in Chapter 4.1. The efficiency used for the inversion algorithm was the total system efficiency for the signal channel. In Figs. 4.6-4.8, the error bars in the photon numbers is due to systematic error arising from the uncertainty in the transmission efficiency for the signal channel.

Without heralding, the measured photon number distribution is largely vacuum, as shown in Fig. 4.6. As the input pump power is increased, the vacuum begin to decrease while the p_1 component increases. However, even at 50 mW, the distribution is primarily composed of vacuum.

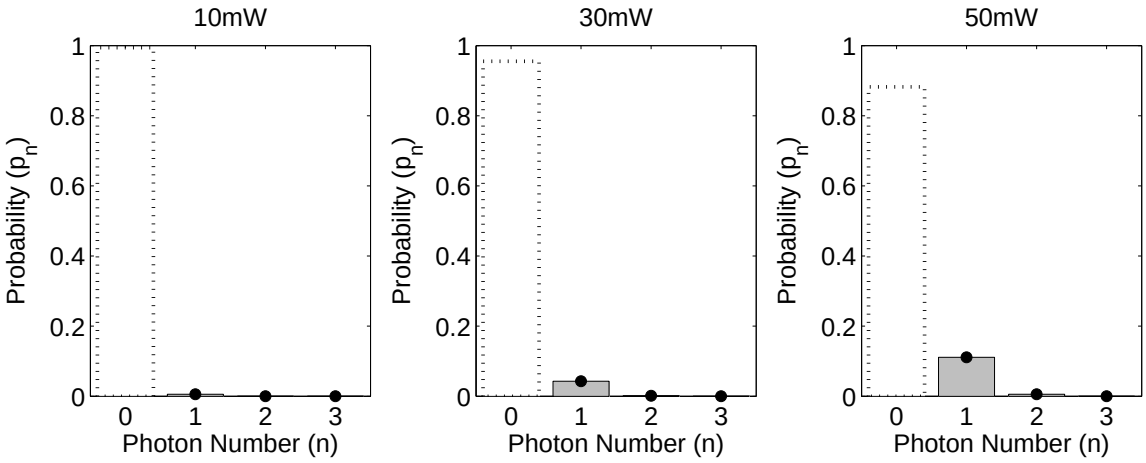

FIGURE 4.6. Photon-number probabilities measured without conditional detection of herald photons. The vacuum component is outlined with a dashed line. Error bars are present and are smaller than the markers.

With a single-herald, the photon number distribution shows a state that is dominated by the one-photon contribution for powers larger than 10 mW. single-heralding effectively selects one photon states. For larger powers, the contributions from two and three photons increase, as expected. The photon number distribution is shown in Fig. 4.7.

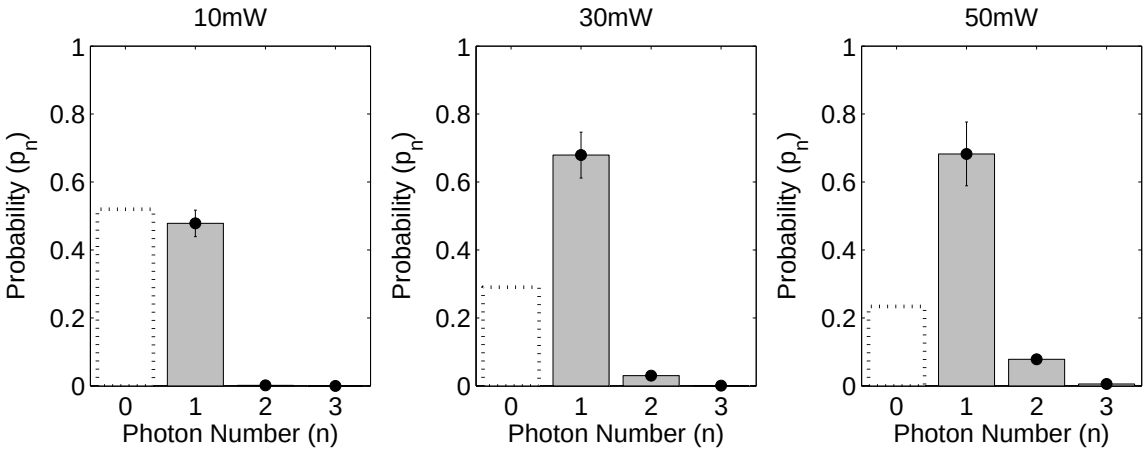

FIGURE 4.7. Photon-number probabilities measured with single herald conditional preparation. The vacuum component is suppressed while the p_1 component is high, showing a dominant one-photon-number component.

Fig. 4.8 experimentally shows the issue with double-heralded photon states. There is a significant one-photon contribution for all powers, due to the presence of noise in the herald channel. With noisy heralding, the occurrences of a single pair and a noise photon will appear to be a two-photon state, but in reality only contains one photon in the signal channel. For the highest power, 50 mW, the two photon component appears to dominate, although the uncertainty in the probabilities is large. The significant error bars result from systematic error in the uncertainty from the efficiency of transmission in the signal channel. The probability for three photons increases slightly with power, as expected.

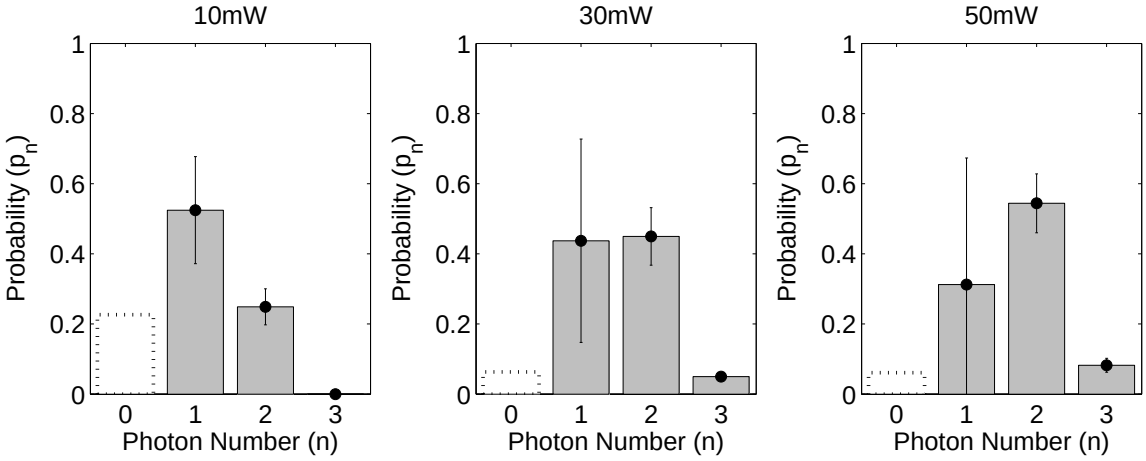

FIGURE 4.8. Photon-number probabilities of double-heralded states. The one-photon contribution is large relative to the two-photon contribution, in contrast to the desired outcome of a pure two-photon state.

Although the double-heralded photon number probability distributions are susceptible to noise, we can use the Klyshko heralding efficiency to determine the noise-free photon number probabilities. By inserting the Klyshko heralding efficiencies from Fig. 4.5 into the inversion algorithm in Eqs. 4.7-4.9 in place of the signal channel transmission efficiency, we are able to recover the photon number

distribution without noise. This method is valid for noise sources uncorrelated with the photon pair generation.

With the Klyshko heralding efficiencies in the inversion algorithm, the photon number distribution is dominated by the probability for a two-photon state at all powers. The distributions are presented in Fig. 4.9. The error bars are due to the statistical uncertainty, assumed to be determined Poisson counting statistics. The significant component in p_1 is attributed to the presence of unwanted noise in the signal channel. The negative probabilities shown in the distributions result from the lack of constraints on the inversion algorithm. In order to ensure that the inversion is producing physically meaningful results, no constraints (i.e. $0 < p_n < 1$) are placed on the probabilities. Since the probabilities are positive within error bars, we are confident in the validity of this method.

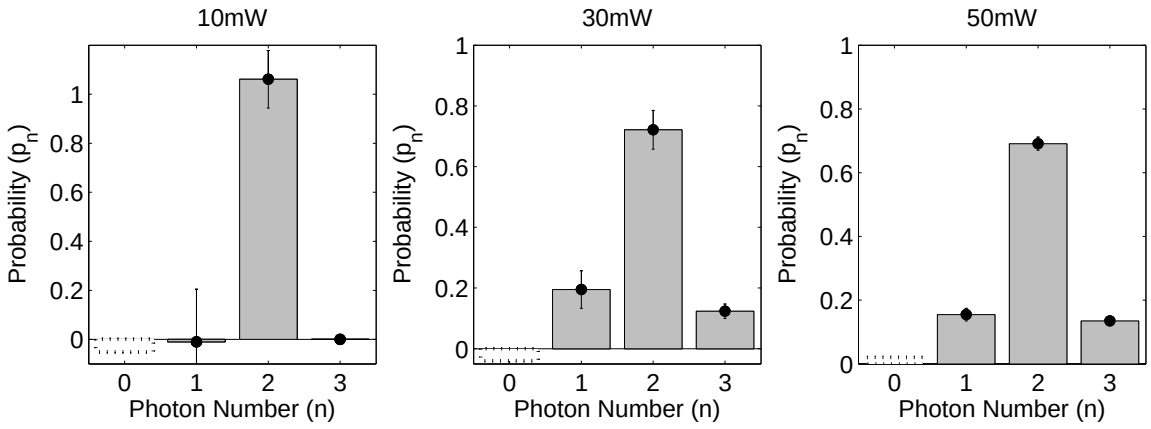

FIGURE 4.9. Inferred noise-free photon-number distributions with double-heralded conditional preparation using the Klyshko heralding efficiencies in the inversion algorithm. The measured values show the photon-number probabilities of the two-photon state that would be observed in the absence of false heralding from independent noise processes.

The fit parameters to the Klyshko heralding efficiency gave insight into the contributions from Raman scattering and pump leakage to the noise in the herald

channel that can be used to determine effective techniques for mitigating the noise, such as cooling the fiber to decrease Raman scattering [102, 103]. From our analysis, it was clear that the dominant contribution to the noise resulted from the pump leakage term, only dependent upon the pump power. Upon further inspection of the filters used in the experimental setup, it was determined that any light from the laser that pumped the titanium sapphire, centered at $\lambda = 532$ nm, would not be adequately filtered out. It was assumed that there would be little contamination of the laser output from the green pump. Following this analysis, a filter to block the 532nm field was inserted at the output of the titanium sapphire laser.

As a result, with the Klyshko heralding efficiency used in the inversion algorithm, the desired two-photon state is recovered. The contributions from p_1 and p_3 are greatly reduced. However, when the system efficiency is used in the inversion mathematics, the noise is still significant. The photon number distributions are shown in Fig. 4.10 for fiber length 2.8 m and input pump power 20 mW.

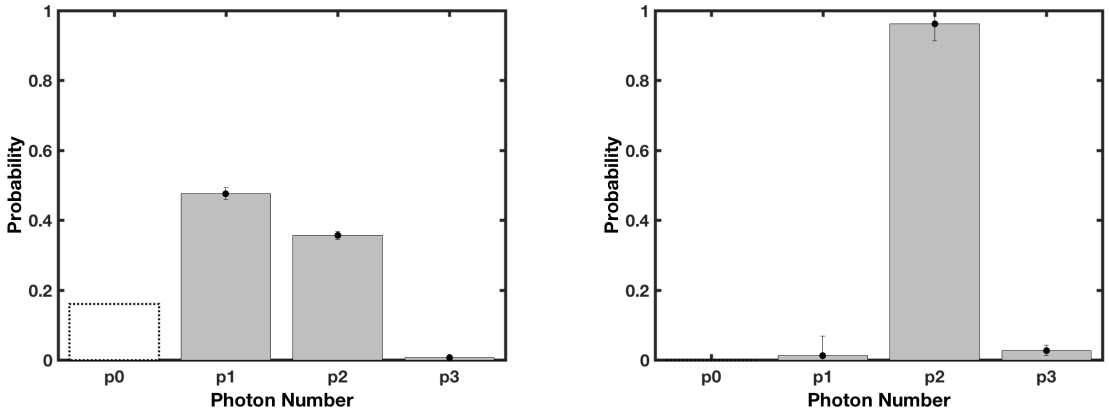

(a) (b)

FIGURE 4.10. Photon number distributions for HB750 fiber of length 2.8 m and input pump power 20 mW. The photon number distribution was calculated by the inversion algorithm with the (a) signal channel transmission efficiency and the (b) Klyshko heralding efficiency.

CHAPTER V

TWO PHOTON BRAGG SCATTERING

Bragg scattering has been shown to be mathematically equivalent to a beamsplitter [69, 104] opening new avenues for creating quantum bits and quantum logic gates [23, 105]. Furthermore, demonstrating Bragg scattering on a two-photon state can provide experimental verification that the process acts as a beamsplitter. With the proper creation and confirmation of a double-heralded two-photon number state, we can experimentally verify the ability of Bragg scattering to act on arbitrary quantum states.

In this chapter, we describe the process using the simplified input-output relations from a typical beamsplitter as shown in of Chapter 3.7. We examine the result of two-photon states on a beamsplitter and the resulting fields. We conclude with experimental considerations and requirements of efficiency to experimentally realize this goal. Some of the work on modified second-order coherence measurements presented in this chapter was carried out in collaboration with Dileep Reddy.

5.1. Input-Output Relations

To describe the process of Bragg scattering with two-photon states, we begin with the standard beamsplitter relations from Fig. 3.7 with inputs $(\hat{a}_1, \hat{a}_2)$ and outputs $(\hat{b}_1, \hat{b}_2)$

$$\hat{a}_1^\dagger = t\hat{b}_1^\dagger + r\hat{b}_2^\dagger \tag{5.1}$$

$$\hat{a}_2^\dagger = -r\hat{b}_1^\dagger + t\hat{b}_2^\dagger. \tag{5.2}$$

In this case, the inputs and outputs correspond to frequencies, with $\hat{a}_1 \mapsto \omega_r$ and $\hat{a}_2 \mapsto \omega_b$. The reflection and transmission coefficients are real and preserve unity, forcing $r^2 + t^2 = 1$. A perfect two-photon state incident in $\hat{a}_1$ becomes the following output state, with a factor of $\frac{1}{\sqrt{2}}$ to preserve normalization:

$$\begin{aligned} |\psi\rangle_{in} &= \frac{\hat{a}_1^\dagger \hat{a}_1^\dagger}{\sqrt{2}} |vac\rangle \\ &= \frac{1}{\sqrt{2}} \left(t\hat{b}_1^\dagger + r\hat{b}_2^\dagger \right)^2 |vac\rangle \\ &= r^2 |0_1 2_2\rangle + \sqrt{2} rt |1_1 1_2\rangle + t^2 |2_1 0_2\rangle . \end{aligned} \tag{5.3}$$

A common measurement in describing quantum states is the second-order coherence measurement of the state, $g^{(2)}$. Typically the state is of the same frequency. We can extend this measurement to the outputs from the Bragg scattering process, where the two frequencies are separated by a dichroic mirror. The photons in each channel are calculated as the expectation value of photons in each beam

$$\langle \hat{n}_{b1} \rangle = 2t^4 + 2r^2 t^2 = 2t^2 (r^2 + t^2) = 2(1 - r^2) \tag{5.4}$$

$$\langle \hat{n}_{b2} \rangle = 2r^4 + 2r^2 t^2 = 2r^2 (r^2 + t^2) = 2r^2. \tag{5.5}$$

The coincidences between the two frequency channels are calculated by the expectation value of both channels having at least one photon

$$\begin{aligned} \langle \hat{n}_{b1} \hat{n}_{b2} \rangle &= \left\langle \hat{b}_1^\dagger \hat{b}_2^\dagger \hat{b}_2 \hat{b}_1 \right\rangle \\ &= 2r^2 t^2 = 2(r^2 - r^4). \end{aligned} \tag{5.6}$$

Combining these results into Eq. 2.66, we can calculate the second-order coherence between the two channels, which is a modified form that is measuring across frequency channels

$$g^{(2)}(0) = \frac{\langle \hat{n}_{b1}\hat{n}_{b2}\rangle}{\langle \hat{n}_{b1}\rangle \langle \hat{n}_{b2}\rangle} = \frac{2r^2(1-r^2)}{4r^2(1-r^2)} = \frac{1}{2}. \tag{5.7}$$

This result is unsurprising for a beamsplitter with a nonzero reflection coefficient, due to the presence of a photon in both channels. This follows Eq. 2.65 for $n = 2$.

As a function of the reflection coefficient of the beam splitter (where $R = r^2$), the coincidences between the two output ports scales as shown in Fig. 5.1. For reflection coefficients (or translation efficiencies) that are close to zero, the coincidences are small. As R increases, more of the state is put into the second output, decreasing the coincidences.

This is not particularly surprising as no new photons are created in the process, but rather photons are changed in frequency. Thus there are two photons in the beam, and a symmetric beamsplitter will equally split the photons and bring the second-order correlation function close to the expected value 1/2 for two photons. Measuring a nonzero second-order coherence between the two frequency channels demonstrates the successful translation through Bragg scattering. However, this does not conclude that the two-photon state is fully translated, but rather the final state could be a combination of one photon in each channel. Ideally, to show the two-photon state is completely translated in frequency, the second-order coherence should go to zero, meaning the two-photons have been translated into the other frequency channel. By measuring the individual frequency channels after Bragg scattering, we can demonstrate the translation of two-photon states with non-unity translation efficiency.

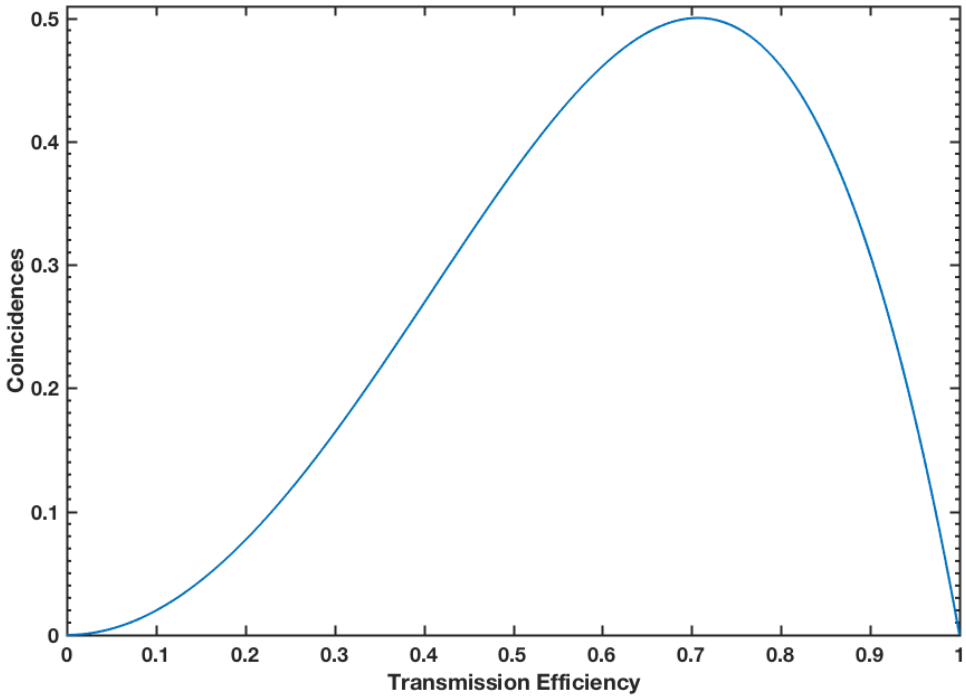

FIGURE 5.1. Coincidences between two output ports from the beam splitter as a function of the square of the reflection coefficient.

5.2. Second-Order Coherences of Individual Channels

For generality, we will assume that the input state is a superposition of both one- and two-photon states. We can write the input state as

$$|\phi\rangle = \beta\,|1\rangle + \gamma\,|2\rangle\,, \tag{5.8}$$

where the coefficients β, γ depend on the properties of the two-color beam splitter, or the frequency translation efficiency and satisfy $|\beta|^2 + |\gamma|^2 = 1$. We assume that there is no vacuum component.

After the input state from Eq. 5.8 is incident upon the fiber for Bragg scattering, the output is calculated by random sampling. The output photon

number distribution from a beam splitter is calculated by use of Bernoulli trials [106]. For an input photon number distribution $p_0(n)$, the output distribution is given by

$$p(m) = \sum_{n=m}^{\infty} \binom{n}{m} T^m (1-T)^{n-m} p_0(n), \tag{5.9}$$

where T is the transmission coefficient of process. This is the same as the process of noisy heralding or a loss in the signal channel from Chapter 4.2. Fig. 5.2 shows the effect of random sampling on different input states for a range of transmission efficiencies. The input photon number distribution is found by taking the taking the inner product with number state

$$p_0(1) = |\langle 1|\phi\rangle|^2 = |\beta|^2 \tag{5.10}$$

$$p_0(2) = |\langle 2|\phi\rangle|^2 = |\gamma|^2. \tag{5.11}$$

For input states that are mostly two-photon states ($|\gamma|^2 > |\beta|^2$), the output photon number distribution contains a significant two-photon component, but only for high transmission efficiencies. For example, if the input state is a perfect two-photon state, the output will appear to be mostly a one-photon state for transmission efficiencies below about 66%. For the case were $|\gamma|^2 = 0.75$ and $|\beta| = 0.25$, the minimum necessary transmission efficiency is higher, around 78%. For the case where the state is equally composed of one-photon and two-photon contributions, the transmission efficiency must be unity in order to see the two-photon contribution.

This presents a significant challenge to demonstrate the translation of a two-photon state since low efficiency will degrade the statistics from two-photon to one-

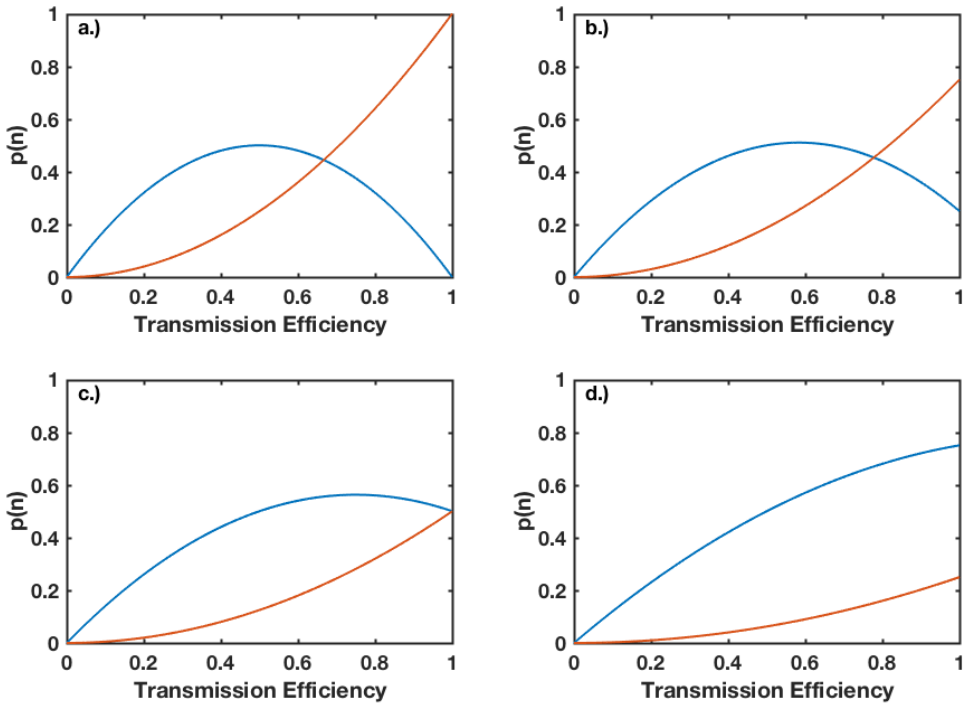

FIGURE 5.2. $p(1)$ (blue lines) and $p(2)$ (red lines) contributions to the photon number distribution of the state after a beamsplitter plotted against the transmission efficiency. The insets define different initial distributions: a.) $p(n) = [0, 1]$; b.) $p(n) = [0.25, 0.75]$; c.) $p(n) = [0.5, 0.5]$; d.) $p(n) = [0.75, 0.25]$; where $p(n) = [p(1), p(2)]$.

photon. However, a measurement of the second-order coherence function for the beam at the output of the Bragg scattering process would appear to have a value of 1/2, regardless of the relative contributions from one- and two-photon states. This results from the presence of any amount of a two-photon state, which tends $g^{(2)}$ away from zero, the value for a true one-photon state. Therefore, it is important to measure the full photon number distribution using multiplexed detectors to accurately determine the statistics of the state.

5.3. Effects of Thresholding Detectors

Furthermore, the use of non-unit efficiency, thresholding detectors adds a level of complexity when properly evaluating the results of second-order coherence measurements. The formulae described above imply perfect number resolving detectors that are making photon number measurements.

The second-order coherence measurements can also be written in general as

$$g^{(2)}(\tau = 0) = \frac{P_{AB}}{P_A P_B}, \tag{5.12}$$

where P_i is the probability for a detection at detector i and P_{ij} is the probability for a coincident detection at i and j. The probabilities of detection follow from those used in the conditional probability matrix for spatially multiplexing. Eq. 4.7 and 4.8 defined the probability for a click given a certain number of photons, but to provide the total probability of a detector clicking, we sum those values over input photons [107, 108]

$$P_A = \sum_{n=1}^{\infty} \mathscr{P}(A|n) = \sum_{n=1}^{\infty} \left[1 - \left(1 - \frac{\eta_A}{2}\right)^n\right] p_0(n) \tag{5.13}$$

$$P_B = \sum_{n=1}^{\infty} \mathscr{P}(B|n) = \sum_{n=1}^{\infty} \left[1 - \left(1 - \frac{\eta_B}{2}\right)^n\right] p_0(n) \tag{5.14}$$

$$\begin{aligned} P_{AB} &= \sum_{n=1}^{\infty} \mathscr{P}(AB|n) \\ &= \sum_{n=1}^{\infty} \left[1 - \left(1 - \frac{\eta_A}{2}\right)^n - \left(1 - \frac{\eta_B}{2}\right)^n + \left(1 - \frac{\eta_A}{2} - \frac{\eta_B}{2}\right)^n\right] p_0(n), \end{aligned} \tag{5.15}$$

where η_i is the detector specific efficiency and the input photon number distribution is $p_0(n)$. The factors of $(1/2)$ multiplied by the efficiencies result from the reflection

and transmission coefficients used in the Hanbury-Brown Twiss setup used to measure the second-order coherence of the beam.

Inserting Eqs. 5.13-5.15 into Eq. 5.12, one finds the modified second-order coherence function, denoted by $\Gamma(0)$. This is measured at $g^{(2)}(\tau = 0)$ for all further equations. Assuming that the input photon number distribution is zero for $n > 3$, the modified second-order coherence function $\Gamma(\tau = 0)$ is

$$\Gamma(0) = \frac{2p_0(2)}{\left[p_0(1) + 2p_0(2)\left(1 - \frac{\eta_A}{4}\right)\right]\left[p_0(1) + 2p_0(2)\left(1 - \frac{\eta_B}{2}\right)\right]}. \tag{5.16}$$

It is clear from Eq. 5.16 that for a perfect one-photon state, $\Gamma(0) = 0$. However, for a perfect two-photon state, the value is not 1/2 as predicted by Eq. 2.65. Even in the case of unit efficiency, $\Gamma(0)$ for a perfect two-photon state is 8/9. The modified second-order coherence function only matches the case of number resolving detectors when the efficiency is zero. $\Gamma(0)$ for different detector efficiencies is shown in Fig. 5.3.

For two detectors with the same efficiency of 60%, the modified second-order coherence does not increase beyond 0.7. The value of $\Gamma(0)$ for different two-photon contributions for detectors at 60% are shown in Fig. 5.4.

Therefore, it is important to take great care when using second-order coherence measurements to determine the contributions from photon numbers larger than 1. Second-order coherence measurements are susceptible to the effects of non-unit efficiency and the thresholding nature of detectors commonly used in quantum optics experiments, such as avalanche photodiodes. Furthermore, it is extremely important to experimentally achieve high conversion efficiencies to demonstrate the translation of two-photon states.

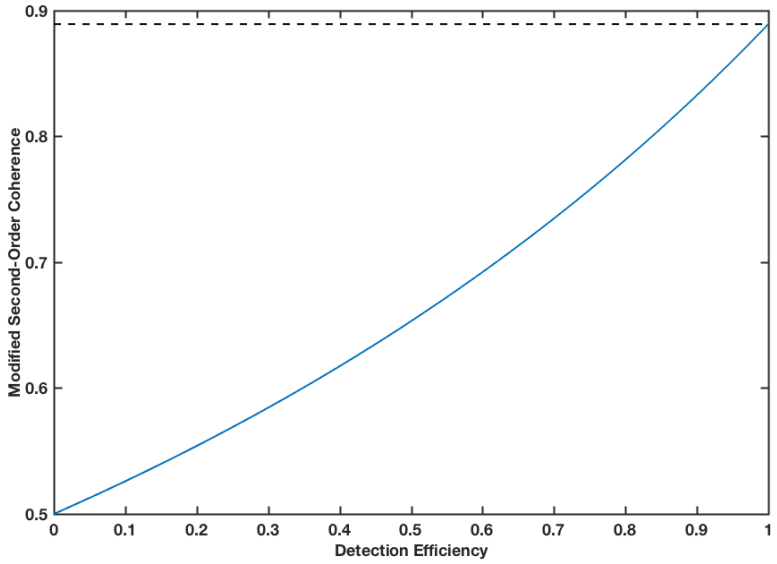

FIGURE 5.3. Modified second-order coherence, $\Gamma(0)$, for different detector efficiencies. The value starts at the theoretical value for number resolving detectors when the detector efficiency is 0 and rises to a value of $8/9$, very close to the classical limit.

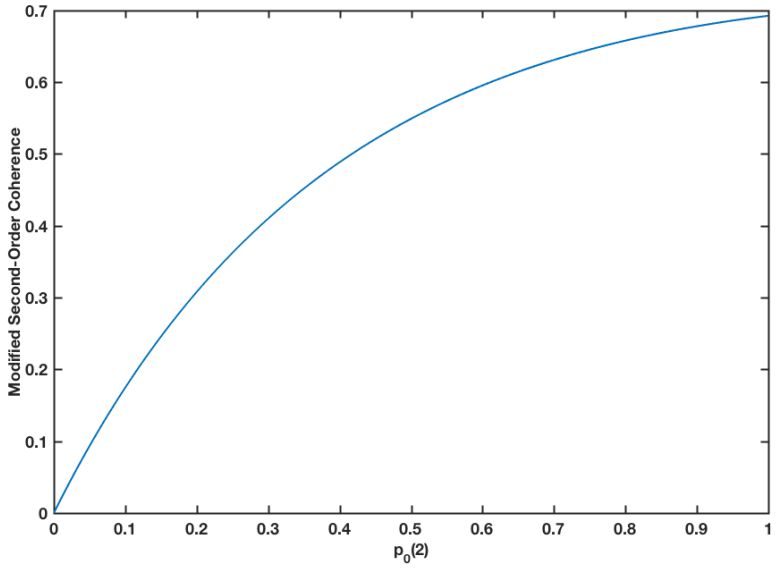

FIGURE 5.4. Calculated modified second-order coherence against the value of the two-photon contribution. It was assumed that the state was comprised of one- and two-photon components, such that $p_0(1) + p_0(2) = 1$.

CHAPTER VI

CONCLUDING REMARKS

In this dissertation, we have explored the process of creating double-heralded two-photon states in optical fibers. Our journey began with a brief description of the formalism of quantum mechanics. We described the quantization of the electric field and the transition into the quantum regime for the simple harmonic oscillator. After some basics on quantum mechanics, we moved to quantum states of light and the different statistics that coherent, number, and thermal states exhibit. Finally, we concluded our discussion of the basics of quantum optics with common measurement schemes.

From quantum optics, we described the optical fibers and the basic methods for describing the behavior of light propagating through a fiber. The invention of the laser, a coherent source with the potential for high intensity fields, along with the dispersion of optical fibers allows for many interesting phenomena to be explored. Nonlinear optics in fibers is a rich and interesting field, into which we provided only a brief glimpse. Specifically, we described the process of creating photon pairs in optical fibers with commercially available, birefringent fibers, quickly becoming a common method for creating photon pairs for quantum optics. Furthermore, we discussed recently developed photonic crystal fibers that have exotic dispersion profiles. As a result many nonlinear effects that were previously restricted to certain frequency regimes are now accessible in a wide and tailorable range of frequencies, depending on the fiber fabrication. In addition, the small core of PCFs lends the fiber to higher energy densities and an enhancement in the magnitude of the nonlinear effects.

Combining quantum optics and nonlinear optics, we explored the process of creating photon pairs larger than 1 in optical fibers. We presented the advantages of heralding when working with a single photon pair. In contrast, the double-heralded photon state is susceptible to the noise processes mitigated through heralding of a single-photon state. We analyzed the noise and showed that the presence of noise in the heralding channel is analogous to a lossy signal channel. The noise in the heralding channel was measured by examining the efficiency to measure coincidences created by photon pairs from our source. The photon pairs were measured by a spatially multiplexed detection setup that provided the photon number distribution. The efficiency of detecting coincidences from the source provides great insight into the noise present in the heralding channel. By varying the average input pump power and the length of the source fiber, we were able to model the noise contributions. Accordingly, this allowed us to determine the relative significance of the noise sources present, providing a direction to further decrease the noise in the heralding channel. Finally, with proper characterization of the noise, we were able to produce the inferred noise-free photon number distribution that would be present in the absence of noise from our source.

After presenting the process for creating a double-heralded two-photon state, we described a method for changing the frequency of the two-photon state. The nonlinear process of Bragg scattering in an optical fiber is analogous to a photon incident upon a moving beamsplitter that imparts a Doppler shift in one channel, but not the other. The process of Bragg scattering can be decomposed as a transformation between the input frequency and the output frequency. We showed the importance of having a high translation efficiency to properly frequency translate a two-photon state. Two-photon states are susceptible to losses in

the experimental apparatus that quickly degrade the statistics. With a lossy system or low efficiencies, the two-photon state will appear to be a one-photon state. Methods for measuring photon number states using thresholding detectors with non-unity efficiency were described. The result of non-unity efficiency and the thresholding nature of the detectors changes the second-order coherence measurements significantly from the case of number resolving, unit-efficiency detectors.

The future of this work requires some care to properly perform frequency translation of two-photon states. First, it is challenging to truly avoid the issue of Raman scattering in the source fiber. From the analysis presented here, it was clear that the dominant noise source were photons from the pump to the titanium sapphire laser. After this frequency was filtered, the double-heralded state still contained a prominent one-photon state. The noise-free distribution was much improved, but the raw data must present a two-photon state before the state created is a true two-photon state.

Second, it is of the utmost importance to improve the input coupling efficiency to the PCF to properly demonstrate a full translation of the input two-photon state. High efficiency is achievable through continued work to increase coupling efficiency into the PCF and finer tailoring of the pump spectrum and fiber length of the source fiber. Although these advancements are technologically challenging, it is possible to realize these changes experimentally, demonstrating a successful translation of two-photon states would definitively show the ability for Bragg scattering to frequency translate arbitrary quantum states of light.

Alternatively, it is possible to experimentally verify that the process of Bragg scattering is analogous to a beam splitter. The expected photon number

distribution after frequency translation depends on the translation efficiency of the BS process. By performing frequency translation on a known photon-number distribution while changing the translation efficiency and measuring the output, it can be shown the output photon-number distribution follows the expected value if the process was a beamsplitter with a varying transmission efficiency. Mapping out the photon-number distributions shown in Chapter V would clearly confirm that the process of BS has the same effect as a beamsplitter, or random sampling of a photon-number distribution.

REFERENCES CITED

[1] W. Heisenberg, *Physics and Philosophy: The Revolution in Modern Science* (Harper Perennial Modern Classics, 2007), 2nd ed.

[2] P. A. Franken, A. E. Hill, C. W. Peters, and G. Weinreich, "Generation of optical harmonics," Phys. Rev. Lett. **7**, 118–119 (1961).

[3] S. E. Harris, M. K. Oshman, and R. L. Byer, "Observation of tunable optical parametric fluorescence," Phys. Rev. Lett. **18**, 732–734 (1967).

[4] D. C. Burnham and D. L. Weinberg, "Observation of simultaneity in parametric production of optical photon pairs," Phys. Rev. Lett. **25**, 84–87 (1970).

[5] R. B. Hanbury and R. Twiss, "Correlation between photons in two coherent beams of light," Nature **177**, 27–29 (1956).

[6] R. J. Glauber, "The quantum theory of optical coherence," Phys. Rev. **130**, 2529–2539 (1963).

[7] H. J. Kimble, M. Dagenais, and L. Mandel, "Photon antibunching in resonance fluorescence," Phys. Rev. Lett. **39**, 691–695 (1977).

[8] R. Short and L. Mandel, "Observation of sub-Poissonian photon statistics," Phys. Rev. Lett. **51**, 384–387 (1983).

[9] P. Grangier, G. Roger, and A. Aspect, "Experimental evidence for a photon anticorrelation effect on a beam splitter: A new light on single-photon interferences," Europhysics Letters **1**, 173 (1986).

[10] C. K. Hong and L. Mandel, "Experimental realization of a localized one-photon state," Phys. Rev. Lett. **56**, 58–60 (1986).

[11] C. H. Bennett and G. Brassard, "Quantum cryptography: Public key distribution and coin tossing," International Conference on Computers, Systems & Signal Processing pp. 175–179 (1984).

[12] A. K. Ekert, "Quantum cryptography based on Bell's theorem," Phys. Rev. Lett. **67**, 661–663 (1991).

[13] T. Jennewein, C. Simon, G. Weihs, H. Weinfurter, and A. Zeilinger, "Quantum cryptography with entangled photons," Phys. Rev. Lett. **84**, 4729–4732 (2000).

[14] D. S. Naik, C. G. Peterson, A. G. White, A. J. Berglund, and P. G. Kwiat, "Entangled state quantum cryptography: Eavesdropping on the Ekert protocol," Phys. Rev. Lett. **84**, 4733–4736 (2000).

[15] W. Tittel, J. Brendel, H. Zbinden, and N. Gisin, "Quantum cryptography using entangled photons in energy-time Bell states," Phys. Rev. Lett. **84**, 4737–4740 (2000).

[16] P. W. Shor, "Polynomial-time algorithms for prime factorization and discrete logarithms on a quantum computer," SIAM J. Comput. **26**, 1484–1509 (1997).

[17] L. K. Grover, "Quantum mechanics helps in searching for a needle in a haystack," Phys. Rev. Lett. **79**, 325–328 (1997).

[18] J. I. Cirac and P. Zoller, "Quantum computations with cold trapped ions," Phys. Rev. Lett. **74**, 4091–4094 (1995).

[19] C. Monroe, D. M. Meekhof, B. E. King, W. M. Itano, and D. J. Wineland, "Demonstration of a fundamental quantum logic gate," Phys. Rev. Lett. **75**, 4714–4717 (1995).

[20] D. G. Cory, A. F. Fahmy, and T. F. Havel, "Ensemble quantum computing by NMR spectroscopy," PNAS **94**, 1634–1639 (1997).

[21] N. A. Gershenfeld and I. L. Chuang, "Bulk spin-resonance quantum computation," Science **275**, 350–356 (1997).

[22] J. A. Jones, M. Mosca, and R. H. Hansen, "Implementation of a quantum search algorithm on a quantum computer," Nature **393**, 344–346 (1998).

[23] E. Knill, R. Laflamme, and G. J. Milburn, "A scheme for efficient quantum computation with linear optics," Nature **409**, 46–52 (2001).

[24] T. B. Pittman, M. J. Fitch, B. C. Jacobs, and J. D. Franson, "Experimental controlled-not logic gate for single photons in the coincidence basis," Phys. Rev. A **68**, 032316 (2003).

[25] J. J. O'Brien, "Demonstration of an all-optical quantum controlled-not gate," Nature **426**, 264–267 (2003).

[26] K. C. Kao and G. A. Hockham, "Dielectric-fibre surface waveguides for optical frequencies," Proceedings of the Institution of Electrical Engineers **113**, 1151–1158 (1966).

[27] K. Garay-Palmett, R. Rangel-Rojo, and A. B. U'Ren, "Tailored photon pair preparation relying on full group velocity matching in fiber-based spontaneous four-wave mixing," J. of Mod. Opt. **55**, 3121–3131 (2008).

[28] B. J. Smith, P. Mahou, O. Cohen, J. S. Lundeen, and I. Walmsley, "Photon pair generation in birefringent optical fibers," Opt. Express **17**, 23589–23602 (2009).

[29] B. Fang, O. Cohen, and V. O. Lorenz, "Polarization-entangled photon-pair generation in commercial-grade polarization-maintaining fiber," J. Opt. Soc. Am. B **31**, 277–281 (2014).

[30] E. Meyer-Scott, V. Roy, J.-P. Bourgoin, B. L. Higgins, L. K. Shalm, and T. Jennewein, "Generating polarization-entangled photon pairs using cross-spliced birefringent fibers," Opt. Express **21**, 6205–6212 (2013).

[31] V. O. Lorenz, B. Fang, and O. Cohen, "Generation of polarization-entangled photons in a standard polarization-maintaining fiber," Journal of Physics: Conference Series **414**, 012007 (2013).

[32] J. Fan and A. Migdall, "Generation of cross-polarized photon pairs in a microstructure fiber with frequency-conjugate laser pump pulses," Opt. Express **13**, 5777–5782 (2005).

[33] J. Fulconis, O. Alibart, W. J. Wadsworth, P. S. J. Russell, and J. G. Rarity, "High brightness single mode source of correlated photon pairs using a photonic crystal fiber," Opt. Express **13**, 7572–7582 (2005).

[34] J. G. Rarity, J. Fulconis, J. Duligall, W. J. Wadsworth, and P. S. J. Russell, "Photonic crystal fiber source of correlated photon pairs," Opt. Express **13**, 534–544 (2005).

[35] J. Fulconis, O. Alibart, J. O'Brien, W. Wadsworth, and J. Rarity, "Nonclassical interference and entanglement generation using a photonic crystal fiber pair photon source," Phys. Rev. Lett. **99**, 120501 (2007).

[36] M. Halder, J. Fulconis, B. Cemlyn, A. Clark, C. Xiong, W. J. Wadsworth, and J. G. Rarity, "Nonclassical 2-photon interference with separate intrinsically narrowband fibre sources," Opt. Express **17**, 4670–4676 (2009).

[37] H. J. McGuinness, M. G. Raymer, C. J. McKinstrie, and S. Radic, "Quantum frequency translation of single-photon states in a photonic crystal fiber," Phys. Rev. Lett. **105**, 093604 (2010).

[38] L. T. Troland, "On the measurement of visual stimulation intensities," J. of Exp. Psych. **2**, 1–33 (1917).

[39] G. N. Lewis, "The conservation of photons," Nature **118**, 874–875 (1926).

[40] H. Kragh, "Photon: New light on an old name," ArXiv e-prints 1401.0293 [physics.hist-ph] (2014).

[41] D. J. Griffiths, *Introduction to Quantum Mechanics* (Pearson Education, Inc., 2005), 2nd ed.

[42] J. J. Sakurai, *Modern Quantum Mechanics* (Addison-Wesley Publishing Company, Inc., 1994).

[43] R. Loudon, *The Quantum Theory of Light* (Oxford University Press, Oxford, 2000), 3rd ed.

[44] D. Walls and G. Milburn, *Quantum Optics* (Springer, 2008).

[45] M. Fox, *Quantum Optics: An Introduction* (Oxford University Press, 2006).

[46] M. Beck, "Comparing measurements of $g^{(2)}(0)$ performed with different coincidence detection techniques," J. Opt. Soc. Am. B **24**, 2972–2978 (2007).

[47] J. A. Buck, *Fundamentals of Optical Fibers* (John Wiley & Sons, Inc., 2004), 2nd ed.

[48] G. P. Agrawal, *Nonlinear Fiber Optics* (Academic Press, Oxford, 2006), 4th ed.

[49] J. C. Knight, T. A. Birks, P. S. J. Russell, and D. M. Atkin, "All-silica single-mode optical fiber with photonic crystal cladding," Opt. Lett. **21**, 1547–1549 (1996).

[50] K. Garay-Palmett, H. J. McGuinness, O. Cohen, J. S. Lundeen, R. Rangel-Rojo, A. B. U'ren, M. G. Raymer, C. J. McKinstrie, S. Radic, and I. A. Walmsley, "Photon pair-state preparation with tailored spectral properties by spontaneous four-wave mixing in photonic-crystal fiber," Opt. Express **15**, 14870–14886 (2007).

[51] J. C. Knight, T. A. Birks, P. S. J. Russell, and J. P. D. Sandro, "Properties of photonic crystal fiber and the effective index model," J. Opt. Soc. Am. A **15**, 748–752 (1998).

[52] T. A. Birks, J. C. Knight, and P. S. J. Russell, "Endlessly single-mode photonic crystal fiber," Opt. Lett. **22**, 961–963 (1997).

[53] G. K. Wong, A. Y. Chen, S. Ha, R. Kruhlak, S. Murdoch, R. Leonhardt, J. Harvey, and N. Joly, "Characterization of chromatic dispersion in photonic crystal fibers using scalar modulation instability," Opt. Express **13**, 8662–8670 (2005).

[54] J. D. Jackson, *Classical Electrodynamics* (John Wiley & Sons, Inc., 1999), 3rd ed.

[55] F. Shimizu, "Frequency broadening in liquids by a short light pulse," Phys. Rev. Lett. **19**, 1097–1100 (1967).

[56] R. H. Stolen and C. Lin, "Self-phase-modulation in silica optical fibers," Phys. Rev. A **17**, 1448–1453 (1978).

[57] M. Corona, K. Garay-Palmett, and A. B. U'Ren, "Experimental proposal for the generation of entangled photon triplets by third-order spontaneous parametric downconversion in optical fibers," Opt. Lett. **36**, 190–192 (2011).

[58] M. Raymer, J. Noh, K. Banaszek, and I. Walmsley, "Pure-state single-photon wave-packet generation by parametric down-conversion in a distributed microcavity," Phys. Rev. A **72**, 023825 (2005).

[59] C. J. McKinstrie, S. Radic, and A. R. Chraplyvy, "Parametric amplifiers driven by two pump waves," IEEE J. Sel. Topics Quantum Electron. **8**, 538–547 (2002).

[60] L. Mandel and E. Wolf, *Optical Coherence and Quantum Optics* (Cambridge University Press, 1995), 2nd ed.

[61] Y. H. Chen, G. K. L. Wong, S. G. Murdoch, R. Leonhardt, J. D. Harvey, J. C. Knight, W. J. Wadsworth, and P. S. J. Russell, "Widely tunable optical parametric generation in a photonic crystal fiber," Opt. Lett. **30**, 762–76olen4 (2005).

[62] R. Boyd, *Nonlinear Optics* (Academic Press, 2008), 3rd ed.

[63] R. H. Stolen, M. A. Bösch, and C. Lin, "Phase matching in birefringent fibers," Opt. Lett. **6**, 213–215 (1981).

[64] Q. Lin, F. Yaman, and G. P. Agrawal, "Photon-pair generation by four-wave mixing in optical fibers," Opt. Lett. **31**, 1286–1288 (2006).

[65] Q. Lin, F. Yaman, and G. P. Agrawal, "Photon-pair generation in optical fibers through four-wave mixing: Role of Raman scattering and pump polarization," Phys. Rev. A **75**, 023803 (2007).

[66] L. Cui, X. Li, and N. Zhao, "Minimizing the frequency correlation of photon pairs in photonic crystal fibers," New J. Phys. **14** (2012).

[67] C. Söller, O. Cohen, B. Smith, I. Walmsley, and C. Silberhorn, "High-performance single-photon generation with commercial-grade optical fiber," Phys. Rev. A **83**, 031806(R) (2011).

[68] C. McKinstrie, M. Yu, M. G. Raymer, and S. Radic, "Quantum noise properties of parametric processes," Opt. Express **13**, 4986–5012 (2005).

[69] M. Raymer, S. van Enk, C. McKinstrie, and H. McGuinness, "Interference of two photons of different color," Opt. Comm. **283**, 747–752 (2010).

[70] C. J. McKinstrie, "Unitary and singular value decompositions of parametric processes in fibers," Opt. Comm. **282**, 583–593 (2009).

[71] W. Wasilewski and M. Raymer, "Pairwise entanglement and readout of atomic-ensemble and optical wave-packet modes in traveling-wave Raman interactions," Phys. Rev. A. **73**, 063816 (2006).

[72] T. Opatrný, G. Kurizki, and D. G. Welsch, "Improvement on teleportation of continuous variables by photon subtraction via conditional measurement," Phys. Rev. A. **61**, 032302 (2000).

[73] A. M. Brańczyk, T. C. Ralph, W. Helwig, and C. Silberhorn, "Optimized generation of heralded Fock states using parametric down-conversion," New J. Phys. **12**, 063001 (2010).

[74] H. Takesue, H. Fukuda, T. Tsuchizawa, T. Watanabe, K. Yamada, Y. Tokura, and S. ichi Itabashi, "Generation of polarization entangled photon pairs using silicon wire waveguide," Opt. Express **16**, 5721–5727 (2008).

[75] X. Zhang, I. Jizan, J. He, A. S. Clark, D. Y. Choi, C. J. Chae, B. J. Eggleton, and C. Xiong, "Enhancing the heralded single-photon rate from a silicon nanowire by time and wavelength division multiplexing pump pulses," Opt. Lett. **40**, 2489–2492 (2015).

[76] E. A. Goldschmidt, M. D. Eisaman, J. Fan, S. V. Polyakov, and A. Migdall, "Spectrally bright and broad fiber-based heralded single-photon source," Phys. Rev. A. **78**, 013844 (2008).

[77] A. R. McMillan, J. Fulconis, M. Halder, C. Xiong, J. G. Rarity, and W. J. Wadsworth, "Narrowband high-fidelity all-fibre source of heralded single photons at 1570 nm," Opt. Express **17**, 6156–65 (2009).

[78] D. Achilles, C. Silberhorn, and I. A. Walmsley, "Direct, loss-tolerant characterization of nonclassical photon statistics," Phys. Rev. Lett. **97**, 043602 (2006).

[79] M. N. O'Sullivan, K. W. C. Chan, V. Lakshminarayanan, and R. W. Boyd, "Conditional preparation of states containing a definite number of photons," Phys. Rev. A. **77**, 023804 (2008).

[80] X. Li, J. Chen, P. Voss, J. Sharping, and P. Kumar, "All-fiber photon-pair source for quantum communications: Improved generation of correlated photons," Opt. Express **12**, 3737–3744 (2004).

[81] J. E. Sharping, K. F. Lee, M. A. Foster, A. C. Turner, B. S. Schmidt, M. Lipson, A. L. Gaeta, and P. Kumar, "Generation of correlated photons in nanoscale silicon waveguides," Opt. Express **14**, 12388–12393 (2006).

[82] J. Rarity, P. Tapster, and E. Jakeman, "Observation of sub-Poissonian light in parametric downconversion," Opt. Comm. **62**, 201–206 (1987).

[83] D. Smithey, M. Beck, and M. Raymer, "Measurement of the Wigner distribution and the density matrix of a light mode using optical homodyne tomography: Application to squeezed states and the vacuum," Phys. Rev. Lett. **70**, 1244–1247 (1993).

[84] M. Munroe, D. Boggavarapu, M. E. Anderson, and M. G. Raymer, "Photon-number statistics from the phase-averaged quadrature-field distribution: Theory and ultrafast measurement," Phys. Rev. A **52**, R924–R927 (1995).

[85] A. I. Lvovsky, H. Hansen, T. Aichele, O. Benson, J. Mlynek, and S. Schiller, "Quantum state reconstruction of the single-photon Fock state," Physical Review Letters **87**, 050402 (2001).

[86] A. Ourjoumtsev, R. Tualle-Brouri, and P. Grangier, "Quantum homodyne tomography of a two-photon Fock state," Phys. Rev. Lett. **96**, 213601 (2006).

[87] R. A. Smith, D. V. Reddy, D. L. P. Vitullo, and M. G. Raymer, "Double-heralded generation of two-photon-states by spontaneous four-wave-mixing in the presence of noise," Opt. Express **24**, 5809–5821 (2016).

[88] P. G. Kwiat, A. M. Steinberg, R. Y. Chiao, P. H. Eberhard, and M. D. Petroff, "High-efficiency single-photon detectors," Phys. Rev. A **48**, R867–R870 (1993).

[89] M. J. Fitch, B. C. Jacobs, T. B. Pittman, and J. D. Franson, "Photon-number resolution using time-multiplexed single-photon detectors," Physical Review A **68**, 043814 (2003).

[90] J. Řeháček, Z. Hradil, O. Haderka, J. Peřina, and M. Hamar, "Multiple-photon resolving fiber-loop detector," Phys. Rev. A **67**, 061801 (2003).

[91] J. Sperling, W. Vogel, and G. S. Agarwal, "True photocounting statistics of multiple on-off detectors," Physical Review A **85**, 023820 (2012).

[92] R. Chrapkiewicz, "Photon counts statistics of squeezed and multimode thermal states of light on multiplexed onoff detectors," J. Opt. Soc. Am. B **31**, 1–7 (2014).

[93] P. P. Rohde, J. G. Webb, E. H. Huntington, and T. C. Ralph, "Photon number projection using non-number-resolving detectors," New J. Phys. **9**, 0–18 (2007).

[94] E. A. Dauler, A. J. Kerman, B. S. Robinson, J. K. Yang, B. Voronov, G. Goltsman, S. A. Hamilton, and K. K. Berggren, "Photon-number-resolution with sub-30-ps timing using multi-element superconducting nanowire single photon detectors," J. Mod. Opt. **56**, 364–373 (2009).

[95] M. Avenhaus, K. Laiho, M. V. Chekhova, and C. Silberhorn, "Accessing higher order correlations in quantum optical states by time multiplexing," Phys. Rev. Lett. **104**, 063602 (2010).

[96] T. J. Bartley, G. Donati, X.-M. Jin, A. Datta, M. Barbieri, and I. A. Walmsley, "Direct observation of sub-binomial light," Phys. Rev. Lett. **110**, 173602 (2013).

[97] D. Achilles, C. Silberhorn, C. Śliwa, K. Banaszek, I. A. Walmsley, M. J. Fitch, B. C. Jacobs, T. B. Pittman, and J. D. Franson, "Photon-number-resolving detection using time-multiplexing," J. Mod. Opt. **51**, 1499–1515 (2004).

[98] P. Kok and S. L. Braunstein, "Postselected versus nonpostselected quantum teleportation using parametric down-conversion," Phys. Rev. A **61**, 042304 (2000).

[99] D. Klyshko, "Use of two-photon light for absolute calibration of photoelectric detections," Sov. J. Quantum Electron. **10**, 1112–1117 (1980).

[100] M. Ware and A. Migdall, "Single-photon detector characterization using correlated photons: the march from feasibility to metrology," J. Mod. Opt. **51**, 1549–1557 (2004).

[101] S. V. Polyakov and A. L. Migdall, "High accuracy verification of a correlated-photon-based method for determining photon-counting detection efficiency," Opt. Express **15**, 1390–1407 (2007).

[102] H. Takesue and K. Inoue, "1.5-μm band quantum-correlated photon pair generation in dispersion-shifted fiber: Suppression of noise photons by cooling fiber," Opt. Express **13**, 7832–7839 (2005).

[103] S. D. Dyer, M. J. Stevens, B. Baek, and S. W. Nam, "High-efficiency, ultra low-noise all-fiber photon-pair source," Opt. Express **16**, 9966–9977 (2008).

[104] H. J. McGuinness, M. G. Raymer, and C. J. McKinstrie, "Theory of quantum frequency translation of light in optical fiber: application to interference of two photons of different color," Opt. Express **19**, 17876–907 (2011).

[105] P. Kok, K. Nemoto, T. C. Ralph, J. P. Dowling, and G. J. Milburn, "Linear optical quantum computing with photonic qubits," Rev. Mod. Phys. **79**, 135–174 (2007).

[106] B. Saleh and M. Teich, *Fundamentals of Photonics* (John Wiley & Sons, Inc., 2007), 2nd ed.

[107] D. V. Reddy and R. A. Smith, "Number-statistics of two- & three-point correlations with threshold detectors," Internal Report (2014).

[108] D. V. Reddy and R. A. Smith, "Modulation Instability and Double Heralding," Internal Report (2015).